Composites Part B 312 (2026) 113311

Contents lists available at ScienceDirect

Composites Part B

journal homepage: www.elsevier.com/locate/composites

Numerical analysis of uncertainty propagation in short fiber-reinforced composites: From injection molding to material testing

Nicolas Christ [a,*], Florian Wittemann [b], Benedikt Rohrmüller [a], Jörg Hohe [a], Luise Kärger [b], Carla Beckmann [a]

[a] Fraunhofer Institute for Mechanics of Materials IWM, 79108, Freiburg, Germany
[b] Karlsruhe Institute of Technology, 76131, Karlsruhe, Germany

ARTICLE INFO

Keywords:
Short fiber composites
Uncertainty quantification
Fiber orientation
Process chain
Probabilistic simulation

ABSTRACT

The present study investigates a novel methodology for the numerical assessment of uncertainties and their propagation in injection-molded fiber-reinforced polymers (FRPs). Focusing on two primary sources of uncertainty, which are the microstructural variability due to injection molding process parameters and inherent material scatter, the research examines their individual contributions to the scattering of effective properties, specifically the Young's modulus of the composite. A random vector model was used to describe the orientation states across the structure, derived from multiple injection molding simulations with varying input parameter distributions. The scatter of structural material parameters is further built upon a joint distribution between orientation concentration and constitutive parameters. The results reveal that while the overall orientation states exhibited less scatter than expected, a clear relationship emerged between the concentration of injection molding parameters and the cumulative distribution functions (CDFs) of effective modulus, indicating non-linear interactions between orientation and material scatter. Additionally, the analysis highlighted the increased sensitivity of scattering behavior based on sample orientation, emphasizing the effect of geometry on flow properties. This research underscores the complex interplay of uncertainties in determining effective material behavior, suggesting that future studies should explore a broader range of input parameters and refine distribution assumptions. The findings provide valuable insights for advancing the design and manufacturing processes of polymer composites, establishing a foundation for more comprehensive analyses of uncertainty in material properties.

1. Introduction

Structures and components made of injection-molded short fiber composites are widely used in many fields of modern lightweight construction. Discontinuously short fiber-reinforced composites combine light weight with reasonable stiffness and strength on the one hand with the ability to use standard industrial-scale high-throughput processes such as injection molding on the other hand. Another advantage is the ability for the easy design of structures with rather complex shapes, including local functionalizations like ribs or load-point support structures. Short fiber composites are mostly found in semi-structural applications, however, Keyser et al. [1] showed that modern short fiber-reinforced thermosetting materials might exhibit similar properties as standard aluminum alloys.

As for all composite materials, the material response of discontinuously short fiber-reinforced plastics and structures consisting thereof strongly depends on their microstructure. Consequently, a vast body of literature on the interrelation between microstructure and macroscopic material properties for this class of material has been developed over the past decades. Now classical studies have been provided – among others – by Aboudi [2], Hashin [3] or Hill [4] to mention just a few. The macroscopic material response of short fiber-reinforced materials is governed by several properties and mechanisms on the microstructural level. One of the most important effects on the microscale is the effect of the fiber orientation distribution, studied exhaustively by Advani and Tucker [5] already in 1987, introducing the concept of fiber orientation tensors for quantification of the properties of disordered short fiber microstructures. The effect of the fiber length has first been analyzed by Laws and McLaughlin [6]. The discontinuous type of the fiber-reinforcement causes the development of inhomogeneous stress and strain distributions on the microscale with stress concentrations especially around the fiber ends, triggering failure to emanate from these sites (e.g. Jiang et al. [7]). The interaction of neighboring fibers and

* Fraunhofer Institute for Mechanics of Materials IWM, Wöhlerstraße 11, 79108 Freiburg, Germany
E-mail address: nicolas.christ@iwm.fraunhofer.de (N. Christ).

https://doi.org/10.1016/j.compositesb.2025.113311
Received 17 July 2025; Received in revised form 29 September 2025; Accepted 10 December 2025
Available online 19 December 2025

especially the effects of fillers distributed through the polymeric matrix as a third phase on the microstructural level have been investigated by Yu and Bhattacharyya [8]. Further relevant effects might be caused by the constituents themselves, such as the degree of crystallinity of thermoplastic matrix systems, as shown in a recent contribution by Wetzel et al. [9] based on a homogenization analysis considering a representative volume element for the microstructure. This study reveals again that the polymerization of chemically identical matrix systems might be different between the fibers and when processed as neat polymer.

Homogenization analyses such as those presented in this study and many others are frequently employed to determine elastic or elastic plastic material properties for numerical simulations of the composite material on the macroscale. Whereas elastic effective material models were used in the early contributions, more recent studies mostly employ elastic plastic material models as already used, e.g., by Lusti et al. [10] or Ji and Wang [11]. In recent years, the direct coupling of bottom-up multiscale and homogenization analyses with structural simulations and in corresponding top-down approaches in terms of integrated computational materials engineering analyses became increasingly popular (e.g., Li et al. [12]). An approach of this type has been presented, for example, by Kärger et al. [13] for continuously fiber-reinforced composites manufactured by means of a resin transfer molding process. Scimieri et al. [14] and Mayer et al. [15] proposed specific mapping algorithms for the transfer of the results between the different finite element meshes employed in the individual simulation steps, especially for the transfer of the molding results onto meshes for the solid body analysis. In the field of discontinuously fiber-reinforced composites, Buck et al. [16] used an integrated computational materials engineering approach to study process effects on the structural response, with special interest directed at the fiber orientation distributions. Görthofer et al. [17] provided an integrated process chain analysis for sheet molding compounds manufactured in a compression molding process. A similar study, however, directed to injection-molded short fiber-reinforced thermosetting materials has been provided by Reclusado and Nagasawa [18].

A specific feature of short fiber-reinforced composites is their disordered microstructure, resulting in pronounced uncertainties in their macroscopic material response, as already mentioned by Bijsterbosch and Gaymans [19]. Due to their microstructural disorder, the materials feature "true" physical or aleatoric uncertainties in addition to epistemic uncertainties in terms of measurement or modeling inaccuracies (Sriramula and Chryssanthopoulos [20]). To quantify the aleatoric uncertainties, Nguyen and Khaleel [21] employed a probabilistic homogenization approach based on the Eshelby method in conjunction with an ensemble averaging technique. A similar approach has been provided more recently by Sharma et al. [22]. A comprehensive overview of the causes and propagation of uncertainties in injection molded composites, albeit for natural fibers, is given by Proy et al. [23]. They divide the causes of uncertainties into measurement uncertainty, model uncertainty and physical variability and highlight the important role of uncertainty quantification, uncertainty modeling, uncertainty propagation and finally uncertainty management, which this paper effectively addresses. The present authors proposed a probabilistic material model for discontinuously fiber-reinforced materials (Hohe et al. [24]). In a recent contribution by Reiner [25], the uncertainties in the in-plane fracture toughness of laminated composites are analyzed.

Only a few approaches to the transition of uncertainties from the microstructure up to the structural level are available. Soize [26] analyzed the uncertainties in the response of structures consisting of random micro-heterogeneous materials using a random field model for the macroscopic material response based on a Karhunen-Loève expansion. A similar approach has been provided by Rahman and Chakraborty [27] using the Mori–Tanaka mean field homogenization for determination of the macroscopic material properties. An alternative probabilistic strategy for probabilistic simulation on the macroscopic level has been proposed by Ma et al. [28], using a random factor approach. Other studies evaluate individual aspects of the entire process stochastically, such as in Ghauch et al. [29], whereas other studies consider the entire process but without taking variability into account, as in Zaidani et al. [30] or Mu et al. [31]. So far, there is no integrated probabilistic analysis of the structural response due to uncertainties in the process itself up to the structural level, which highlights the specificity of this work.

The present study is concerned with a comprehensive stochastic process chain simulation of short fiber composites with a thermoset matrix. The starting point is a probabilistic process simulation of the thermoset injection molding process based on a prescribed variability of the pressure and temperature as the main process parameters (Wittemann et al. [32]). As a result, the tensor field of the second order fiber orientation tensor and its variability are available. In a second step, the stochastic correlation between microstructure and macroscopic material properties is established, utilizing the stochastic homogenization procedure from a previous contribution by the present authors (Rohrmüller et al. [33]). Using both results as uncertain input, a stochastic mechanical simulation on the structural level is performed in terms of a Monte Carlo simulation, adopting the concept of conditional probability (Ackerman et al. [34]). The approach is demonstrated on the example of a short glass fiber-reinforced composite with a phenolic resin matrix, studied experimentally in a preceding contribution (Wittemann et al. [32], Rohrmüller et al. [33,35]) by the present authors.

2. Stochastic approaches for FRP

Fiber distribution and orientation tensors

The directional dependence of the material properties of FRP is due to the elongated shape of the fibers. If all fibers are oriented in the same direction, there is a strong reinforcing effect for this direction (assuming that the fiber material is stiffer than the matrix material), while the orthogonal directions show hardly any reinforcement. If, on the other hand, the fibers are evenly distributed over the unit sphere, the effective material properties are quasi-isotropic [36, p. 101 ff.].

On the mesoscopic and macroscopic scales, fibers are usually not discretized individually, but they are considered in an average or statistical sense. For this, the fiber orientation distribution function $\psi(\alpha, \beta)$ is introduced, which is a probability density function. It is defined such that the probability of any fiber pointing within a range of the two spherical angles $\alpha \in [\alpha^*, \alpha^* + \mathrm{d}\alpha]$ and $\beta \in [\beta^*, \beta^* + \mathrm{d}\beta]$ is

$$\begin{aligned}&\mathcal{P}(\alpha^* \le \alpha < \alpha^* + \mathrm{d}\alpha, \beta^* \le \beta < \beta^* + \mathrm{d}\beta)\\&= \psi(\alpha^*, \beta^*) \sin\alpha^* \mathrm{d}\alpha \mathrm{d}\beta,\end{aligned} \tag{1}$$

[37, p. 14]. Since the fiber orientation distribution function is usually not known exactly, it is handy to resort to a tensorial average, which is the group of orientation tensors. Here, only the fiber orientation tensor of second order is of interest, which is defined as

$$\begin{aligned}\mathbb{N} &= \int_{\alpha=0}^{\pi} \int_{\beta=0}^{2\pi} \psi(\alpha, \beta) \boldsymbol{p} \otimes \boldsymbol{p} \sin\alpha \mathrm{d}\alpha \mathrm{d}\beta,\\&= \oint \psi(\boldsymbol{p}) \boldsymbol{p} \otimes \boldsymbol{p} \mathrm{d}\boldsymbol{p},\end{aligned} \tag{2}$$

where $\boldsymbol{p}$ are all possible directions in the unit sphere

$$\boldsymbol{p} = \begin{pmatrix} p_1 \\ p_2 \\ p_3 \end{pmatrix} = \begin{pmatrix} \sin\alpha\cos\beta \\ \sin\alpha\sin\beta \\ \cos\alpha \end{pmatrix}, \tag{3}$$

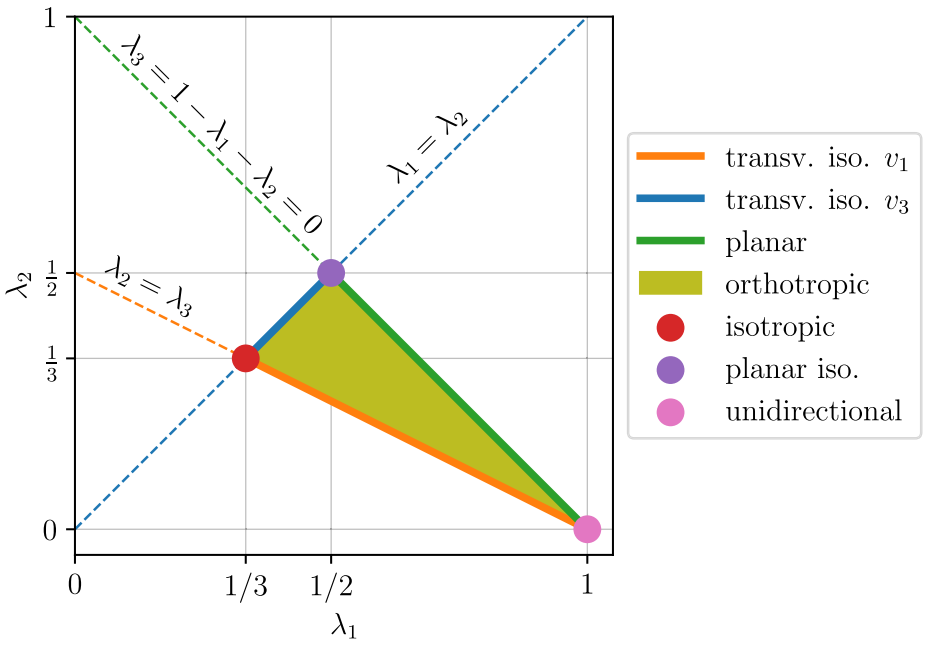

Fig. 1. Orientation triangle to parametrize the orientation state in λ_1 and λ_2 in reference to [41]. All possible orientation states need to lie within the orthotropic triangle or on its boundaries. The corresponding symmetry class in dependence of the orientation state is indicated.

and $\otimes$ is the dyadic tensor product. The orientation tensor $\mathbb{N}$ locally describes the fiber orientation state. The discrete definition of the orientation tensor for m fibers with directions $\boldsymbol{p}_k$ is given with

$$\mathbb{N} = \frac{1}{m} \sum_{k=1}^{m} \boldsymbol{p}_k \otimes \boldsymbol{p}_k. \tag{4}$$

Important properties are that its trace needs to sum up to one and each eigenvalue of $\mathbb{N}$ must take on values between zero and one, which also applies for N_{ij}, for $i = j$. Moreover, the eigenvectors $\boldsymbol{v}_i$ and the corresponding eigenvalues λ_i are the principal directions and principal values of the orientation state, respectively. In other words, the system of eigenvectors of unit length forms an orthonormal coordinate system with orthotropic symmetry. It is common in the literature that the eigenvalues and their corresponding eigenvectors are ordered, so that $\lambda_1 \geq \lambda_2 \geq \lambda_3$ [38]. The interpretation of these characteristics of the orientation state is that a large eigenvalue, e.g., $\lambda_1 \approx 1$, while $\lambda_2 \approx \lambda_3 \approx 0$, indicates strongly aligned fibers in the direction of the first eigenvector. Conversely, when all eigenvalues take on similar values, e.g., $\lambda_1 \approx \lambda_2 \approx \lambda_3 \approx \frac{1}{3}$, the fibers are dispersed equally along the three directions, resulting in a quasi-isotropic orientation state.

With the convention of sorted eigenvalues and the inherent property that $\lambda_3 = 1 - \lambda_1 - \lambda_2$, the space of possible principal values can be parametrized in λ_1 and λ_2 through the orientation triangle [39–41], which is illustrated in Fig. 1. Despite not providing the directions in which fibers are aligned, which need to be tracked separately, the orientation triangle contains the information on material symmetry and degree of alignment. Effective material parameters for FRPs in general depend on the orientation state, so it seems natural to utilize the eigenvalues of the orientation state to estimate these with an appropriate underlying distribution.

Drawing samples from multivariate normal distributions

Throughout this research, simplifying assumptions are made concerning the underlying distributions of the parameters of interest, which include orientation, elastic, and damage parameters. Either the parameters themselves or a transformation of the parameters are assumed to be jointly normally distributed with a mean vector $\boldsymbol{\mu}$ and a covariance matrix $\boldsymbol{\Sigma}$.

In a later stage it will be necessary to draw samples from these distributions which can then be used in the process chain and eventually to evaluate the propagation of uncertainties. To draw samples from these distributions, which are discussed in detail in the following section, a well-known algorithm is utilized [42, p. 65 f.]. The different steps include:

1. Find a root $\boldsymbol{A}$ of the covariance matrix $\boldsymbol{\Sigma}$, so that $\boldsymbol{\Sigma} = \boldsymbol{A}\boldsymbol{A}^\mathsf{T}$. In the present case, the Cholesky decomposition is used.
2. Generate a realization $\boldsymbol{z}$ with the same dimension as the mean vector $\boldsymbol{\mu}$ from an independent standard normal random vector $\boldsymbol{Z} \sim \mathcal{N}(\boldsymbol{0}, \boldsymbol{I})$. Therefore, we use the `numpy.random.normal` implementation of `NumPy` in `Python`.
3. Evaluate $\boldsymbol{x} = \boldsymbol{\mu} + \boldsymbol{A}\boldsymbol{z}$. It can be shown that the realization $\boldsymbol{x}$ of the random vector $\boldsymbol{X}$ is from the same distribution as the random vector of interest, i.e., $\boldsymbol{X} \sim \mathcal{N}(\boldsymbol{\mu}, \boldsymbol{\Sigma})$.

Calculating the conditional probability for normal distributions

It is well known that any distribution for a subset of variables from a multivariate normal, conditional on known values for another subset of variables, is a multivariate normal distribution [43]. When the random vector $\boldsymbol{Z}$ is split into two disjunct subsets

$$\boldsymbol{Z} = \begin{bmatrix} \boldsymbol{Z}_1 \\ \boldsymbol{Z}_2 \end{bmatrix} \tag{5}$$

with corresponding mean

$$\boldsymbol{\mu} = \begin{bmatrix} \boldsymbol{\mu}_1 \\ \boldsymbol{\mu}_2 \end{bmatrix} \tag{6}$$

and covariance

$$\boldsymbol{\Sigma} = \begin{bmatrix} \boldsymbol{\Sigma}_{11} & \boldsymbol{\Sigma}_{12} \\ \boldsymbol{\Sigma}_{21} & \boldsymbol{\Sigma}_{22} \end{bmatrix}, \tag{7}$$

the conditional distribution of $\boldsymbol{Z}_1$ given $\boldsymbol{Z}_2 = \boldsymbol{z}_2$ is

$$\boldsymbol{Z}_1 \mid \boldsymbol{z}_2 \sim \mathcal{N}\left(\boldsymbol{\mu}_{1|2}, \boldsymbol{\Sigma}_{1|2}\right), \tag{8}$$

for which

$$\boldsymbol{\mu}_{1|2} = \boldsymbol{\mu}_1 + \boldsymbol{\Sigma}_{12}\boldsymbol{\Sigma}_{22}^{-1}(\boldsymbol{z}_2 - \boldsymbol{\mu}_2) \tag{9}$$

and

$$\boldsymbol{\Sigma}_{1|2} = \boldsymbol{\Sigma}_{11} - \boldsymbol{\Sigma}_{12}\boldsymbol{\Sigma}_{22}^{-1}\boldsymbol{\Sigma}_{21}. \tag{10}$$

3. Materials and methods

3.1. Reference material

As a reference case for the development of a probabilistic process chain simulation, the material case studied in previous contributions by the present authors is selected. The material is a short glass fiber reinforced phenolic resin matrix composite. The material is supplied in form of plane injection molded rectangular plates with a central sprue position. The material has been investigated with respect to its microstructure and related material properties. In an extensive experimental investigation, being directed especially to the uncertainties in the material response, a large number of specimens of different size, machined from different positions and with different orientations within the available plates was tested (Rohrmüller et al. [35], see also Fig. 4). Further to the mechanical characterization, the microstructural morphology was investigated using metallographic sectioning as well as X-ray computed tomography. Wittemann et al. [32] provided a probabilistic process simulation (see Section 3.2) whereas a probabilistic multiscale simulation has been provided by Rohrmüller et al. [33]. These approaches are utilized here, to study the uncertainty propagation form uncertainties in the process over microstructural uncertainties up to uncertainties in the macroscopic material response.

3.2. Injection molding simulation

The injection molding simulations, used to create the probabilistic cases, are performed with the finite-volume-based software package OpenFOAM and an ongoing interpolation of fiber orientation states. The methodology, mesh, and material models are described in detail in Wittemann et al. [32]. In a first step, a reference process simulation with a filling speed of 75 cm^3/s, tool temperature of 165 °C, material temperature of 120 °C, fiber length of 0.38 mm and initial curing state of 0.06 is performed. Afterwards, 28 further full 3D simulations with varying parameters are performed. Tool and material temperature are varied up to ±10%, in 5% steps. Here, the percent scale refers to the respective reference temperature in °C (so a change of +10% means +16.5 °C). The fiber length and initial curing state are varied up to ±50%, in 10% steps. Based on these 28 simulations, the 100 probabilistic cases are created by interpolation of eigenvectors and eigenvalues of the second order orientation tensor of full 3D simulations [32].

While the valid range of each parameter remains unchanged, in the following different assumptions on the distribution or probability of each parameter within this range is made. These include that each parameter value within this range is equally likely, or that the range is covered by two different normal distributions. The first normal distribution is chosen so that half the range is covered by three standard deviations, i.e., $3\,\sigma$, or six standard deviations, i.e., $6\,\sigma$. In this order, the assumed scatter of the input parameters and consequently the output of the injection molding simulation is reduced. For each assumption, 50 different parameter states are drawn from the given distributions, for which the results of the injection molding simulation are calculated by means of surrogate modeling and interpolation between exact results, as stated in the original paper above.

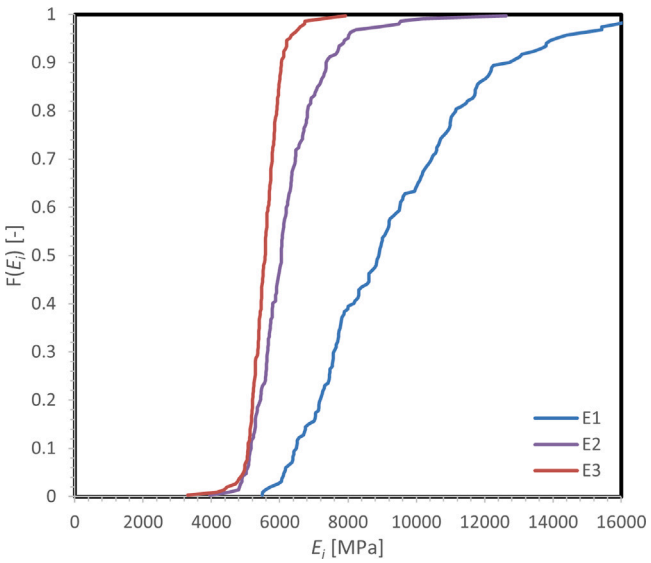

Fig. 2. Probability distributions for the three Young's moduli according to Rohrmüller et al. [33].

3.3. Uncertainties in material properties

To find the joint distribution of orientation and material properties, numerical simulations in the form of representative volume elements (RVEs) that are fitted to the experimental data were performed. The details of this preliminary work is published in a previous contribution (Rohrmüller et al. [33]). Each RVE has dimensions of 0.6 mm × 0.6 mm × 0.1 mm, for which the microstructure, more specifically the fiber distribution, was generated using the methodology proposed by Schneider [44]. After fitting the effective material parameters of the RVEs to experimental data, each RVE is split into 36 equally dimensioned pairwise disjoint subdomains, which are treated as a characteristic of the statistical microstructure. Hence, they are termed statistical volume elements (SVEs). Fig. 2 shows an example for the probability distribution of the uncertain material parameters, here the three Young's moduli. The objective is now to determine the joint distribution of the orientation state and all material parameters.

The set of microstructural and elastic material parameters, which is treated as a vector of random variables $\boldsymbol{Z}^{\mathrm{el}} \in \mathbb{R}^{12\times 1}$, is

$$\boldsymbol{Z}^{\mathrm{el}} = \begin{bmatrix} \lambda_1 \\ \lambda_2 \\ E_1 \\ E_2 \\ E_3 \\ G_{12} \\ G_{13} \\ G_{23} \\ \nu_{12} \\ \nu_{13} \\ \nu_{23} \end{bmatrix}, \tag{11}$$

where λ_1 and λ_2 are the first and second eigenvalues of the orientation tensor ordered by magnitude, i.e., $\lambda_1 \geq \lambda_2 \geq \lambda_3$, E_i are Young's moduli in the direction of the eigenvector $\boldsymbol{v}_i$, G_{ij} are the corresponding shear moduli in the plane spanned by both orientation eigenvectors $\boldsymbol{v}_i$ and

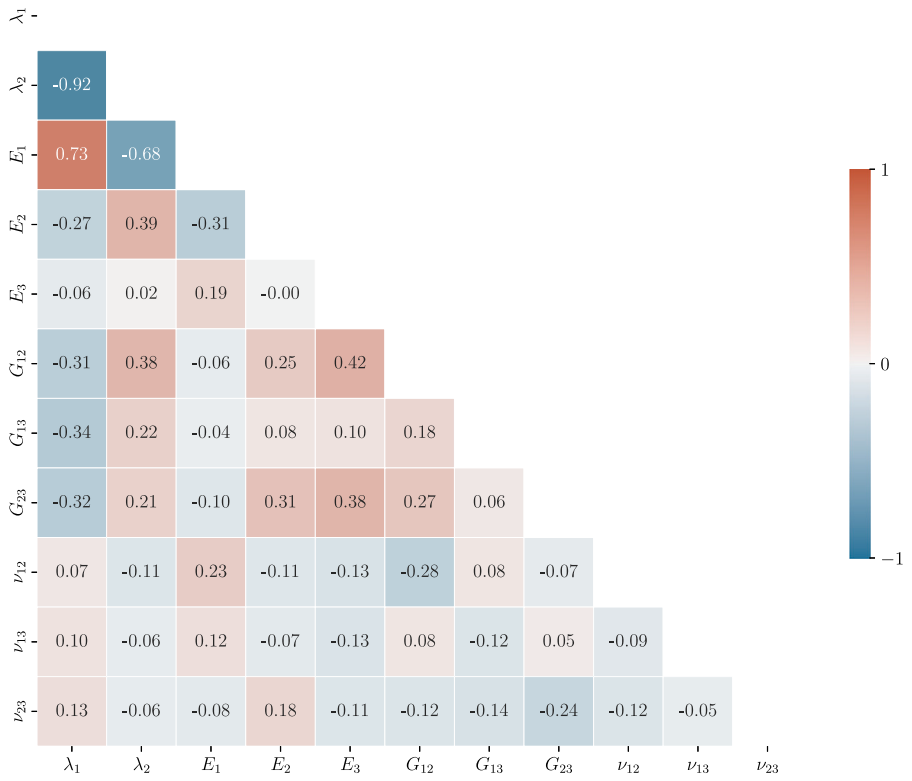

Fig. 3. Correlation matrix between the orientation eigenvalues and elastic parameters, based on the study by Rohrmüller et al. [33].

$\boldsymbol{v}_j$ with normal $\boldsymbol{n} = \boldsymbol{v}_i \times \boldsymbol{v}_j$ and ν_{ij} are Poisson ratios defined through the strain ratios $\nu_{ij} = \varepsilon_{ii}/\varepsilon_{jj}$ (no index summation). Together with the orientation eigenvectors $\boldsymbol{v}_1$, $\boldsymbol{v}_2$ and $\boldsymbol{v}_3 = \boldsymbol{v}_1 \times \boldsymbol{v}_2$, which act as material orientation directions, the set above fully describes the elastic properties of an orthotropic material. Based on the previous study, the correlation matrix of $\boldsymbol{Z}^{\mathrm{el}}$ is visualized in Fig. 3.

Besides elastic properties, damage was modeled in the RVE study using the anisotropic Hill yield criterion, which uses 6 damage variables, i.e., H_{11}, H_{22}, H_{33}, H_{12}, H_{13}, H_{23}. To consider these in the statistical distribution of the material properties, the random vector $\boldsymbol{Z}^{\mathrm{el}}$ is extended to

$$\boldsymbol{Z}^{\mathrm{dmg}} = \begin{bmatrix} \boldsymbol{Z}^{\mathrm{el}\mathsf{T}} & H_{11} & H_{22} & H_{33} & H_{12} & H_{13} & H_{23} \end{bmatrix}^{\mathsf{T}}. \tag{12}$$

The distinction between $\boldsymbol{Z}^{\mathrm{el}}$ and $\boldsymbol{Z}^{\mathrm{dmg}}$ is necessary, because the distribution for each is evaluated on a different data set. While the full database of SVEs provides elastic parameters for $\boldsymbol{Z}^{\mathrm{el}}$, only a subset provides valid damage parameters, which can then be used to evaluate a distribution for $\boldsymbol{Z}^{\mathrm{dmg}}$. SVEs which show no damage cannot be used to fit the damage parameters and hence cannot be used in $\boldsymbol{Z}^{\mathrm{dmg}}$.

For the current study, an assumption is made for each random variable within $\boldsymbol{Z}^{\mathrm{el}}$ and $\boldsymbol{Z}^{\mathrm{dmg}}$, respectively. For simplicity reasons and since many processes in nature follow this distribution, all random variables or a suitable transform are considered to be normally distributed. To prevent unphysical results from being generated, all random variables that cannot take on negative values are first logarithmized. The logarithmized random variable is then assumed to be normally distributed, i.e., the random variable itself is log-normally distributed. Within $\boldsymbol{Z}^{\mathrm{el}}$ and $\boldsymbol{Z}^{\mathrm{dmg}}$ only the Poisson ratios can take negative values. Hence, the transformed random vectors are expressed as

$$\hat{\boldsymbol{Z}}^{\mathrm{el}} = \begin{bmatrix} \log \lambda_1 \\ \log \lambda_2 \\ \log E_1 \\ \log E_2 \\ \log E_3 \\ \log G_{12} \\ \log G_{13} \\ \log G_{23} \\ \nu_{12} \\ \nu_{13} \\ \nu_{23} \end{bmatrix}, \tag{13}$$

and

$$\hat{\boldsymbol{Z}}^{\mathrm{dmg}} = \begin{bmatrix} \hat{\boldsymbol{Z}}^{\mathrm{el}} \\ \log H_{11} \\ \log H_{22} \\ \log H_{33} \\ \log H_{12} \\ \log H_{13} \\ \log H_{23} \end{bmatrix}. \tag{14}$$

As mentioned above, both random vectors are assumed to follow a joint normal distribution

$$\hat{\boldsymbol{Z}}^{\mathrm{el}} \sim \mathcal{N}\left(\boldsymbol{\mu}^{\hat{Z}^{\mathrm{el}}}, \boldsymbol{\Sigma}^{\hat{Z}^{\mathrm{el}}}\right), \tag{15}$$

$$\hat{\boldsymbol{Z}}^{\mathrm{dmg}} \sim \mathcal{N}\left(\boldsymbol{\mu}^{\hat{Z}^{\mathrm{dmg}}}, \boldsymbol{\Sigma}^{\hat{Z}^{\mathrm{dmg}}}\right), \tag{16}$$

for which the mean vectors $\boldsymbol{\mu}^{\hat{Z}^{\mathrm{el}}}$ and $\boldsymbol{\mu}^{\hat{Z}^{\mathrm{dmg}}}$ and the corresponding covariance matrices $\boldsymbol{\Sigma}^{\hat{Z}^{\mathrm{el}}}$ and $\boldsymbol{\Sigma}^{\hat{Z}^{\mathrm{dmg}}}$ are evaluated based on the SVE datasets, respectively.

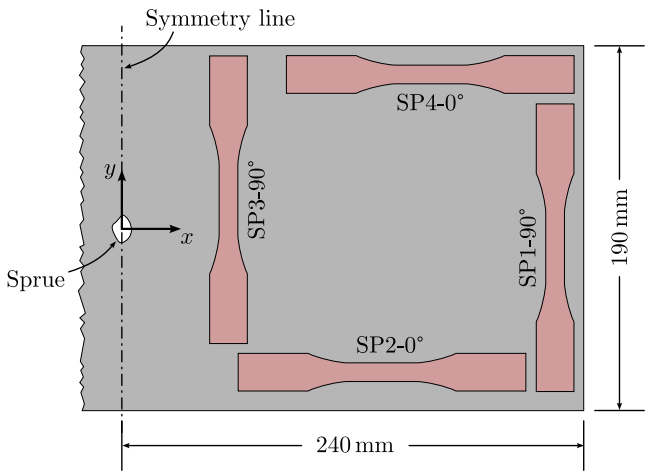

Fig. 4. Tensile specimen positions on one half of the injection-molded plate. The naming consists of the specimen position index and the corresponding orientation in relation to the flow direction, i.e., the global x-coordinate.

3.4. Process chain and uncertainty propagation

As mentioned in Section 3.2, three different types of distributions for the process simulations are considered. These include equally distributed feature characteristics and two normally distributed feature characteristics, in which the chosen range of the equally distributed process parameters is covered by $\pm 3\sigma$ and $\pm 6\sigma$, respectively.

The first step consists of finding the spatial correlation between the orientation states over an entire tensile specimen position within the molded plate, and to draw discrete orientation characteristics from this. The four different specimen positions are depicted on the half plate in Fig. 4. A full description of the experimental investigation of these specimens is given in Rohrmüller et al. [35]. There are two reasons for the vertical and horizontal offset of the individual specimens from the symmetrical center lines. First, additional samples were taken that are not shown here, so that the spatial arrangement shown maximizes the utilization of the plate geometry. Second, this arrangement allows for the consideration of boundary effects and potential asymmetrical filling characteristics. The result of the injection molding simulations is a tuple of orientation states across the plate in the form of an orientation tensor $\mathbb{N}$ for each element of the injection molding simulation. Based on the mentioned properties of $\mathbb{N}$, the orientation state can be parametrized by 5 variables, which are treated as random variables in the following. These are $\{N_{11}, N_{22}, N_{12}, N_{13}, N_{23}\}$.

The injection molding model is discretized in 250 000 elements across the plate. Utilizing the symmetry properties, this can be reduced to half the elements, which in turn creates $5 \cdot 125\,000 = 625\,000$ random variables for the orientation state across half the plate. The corresponding covariance matrix between these random variables would consist of $625\,000^2 \approx 4 \cdot 10^{11}$ entries. Assuming that each variable feature is stored as a `float`, which occupies a storage size of 64 bit, the required storage would exceed 3 TB, which exceeds the available RAM on conventional computing infrastructure. The evaluation of the spatial correlation only over the occupied area of a single test specimen, e.g., SP3-90°, on the injection molding simulation mesh still proved to be too large for the memory available to us. Hence, a data reduction on a coarser mesh is necessary to perform the statistical evaluation.

The final meshing of the tensile specimen is visible in Fig. 5. This mesh is used for the statistical analysis and the structural simulations. In order to draw representative characteristic values for the orientation state, the elastic parameters, and the damage parameters and to investigate the propagation of uncertainties, three distributions must be calculated. These include:

(a) the joint spatial distribution of the five orientation parameters,
(b) the conditional distribution of elastic parameters for observed orientation eigenvalues,
(c) the conditional distribution of damage parameters for observed orientation eigenvalues and elastic parameters.

Based on these distributions, first an orientation state will be drawn for each element of the structural simulation mesh. Based on the drawn two orientation eigenvalues, elastic parameters will be drawn from the conditional distribution, and in a following step, damage parameters will be drawn from a secondary conditional distribution. The drawn material properties are then assigned to the element for an orthotropic material with a material orientation aligned with the drawn orientation eigenvectors.

(a) Joint spatial distribution of orientation parameters

To evaluate the spatial correlation of the five orientation parameters across each specimen position, an information reduction step is necessary first. In this step, the orientation information results from the finely meshed injection molding simulations are mapped to a coarsely meshed structural simulation mesh, which is visible in Fig. 5. For the information reduction, a center point is assigned to each element of both the process and structural simulation mesh, which is equal to the mean coordinate of its nodes. In a subsequent step, for each structural simulation element, the closest process simulation element is calculated by minimizing the respective distances, and its orientation states are adopted from the closest element.

In alignment with the assumptions above, a random vector describing the orientation state for each element across a specimen geometry for a particular specimen position is introduced

$$\hat{\boldsymbol{Z}}^{\mathrm{ori}} = \begin{bmatrix} {}^{1}\log N_{11} \\ {}^{1}\log N_{22} \\ {}^{1}N_{12} \\ {}^{1}N_{13} \\ {}^{1}N_{23} \\ {}^{2}\log N_{11} \\ \vdots \\ {}^{n}\log N_{11} \\ {}^{n}\log N_{22} \\ {}^{n}N_{12} \\ {}^{n}N_{13} \\ {}^{n}N_{23} \end{bmatrix} \in \mathbb{R}^{5n\times 1}, \tag{17}$$

where the preceding superscript represents the uniquely assignable element ID. Moreover,

$$\hat{\boldsymbol{Z}}^{\mathrm{ori}} \sim \mathcal{N}\left(\boldsymbol{\mu}^{\hat{Z}^{\mathrm{ori}}}, \boldsymbol{\Sigma}^{\hat{Z}^{\mathrm{ori}}}\right). \tag{18}$$

The logarithmic transform on the main diagonal components of $\mathbb{N}$ restricts the characteristics to only take on positive values when they are drawn, which is a necessary property of the orientation tensor. Based on the process simulation results, the mean vector and covariance matrix are estimated through

$$\mu_i^{\hat{Z}^{\mathrm{ori}}} = \frac{1}{m}\sum_{k=1}^{m} \hat{z}_{i,k}^{\mathrm{ori}}, \tag{19}$$

where $\hat{z}_{i,k}^{\mathrm{ori}}$ is the kth realization of the ith entry in $\hat{\boldsymbol{Z}}^{\mathrm{ori}}$, and

$$\Sigma_{ij}^{\hat{Z}^{\mathrm{ori}}} = \frac{1}{m-1}\sum_{k=1}^{m}\left(\hat{z}_{i,k}^{\mathrm{ori}} - \mu_i^{\hat{Z}^{\mathrm{ori}}}\right)\left(\hat{z}_{j,k}^{\mathrm{ori}} - \mu_j^{\hat{Z}^{\mathrm{ori}}}\right), \tag{20}$$

with $m = 50$. For the reasons given above, the sample covariance matrix $\boldsymbol{\Sigma}^{\hat{Z}^{\mathrm{ori}}}$ quickly occupies large memory sections for a fine structural mesh.

For the calculated mean and covariance, an arbitrary amount of orientation realizations can be drawn for a given specimen geometry and position. The corresponding algorithm was described in Section 1. Throughout this paper, a total of 20 realizations were drawn for each

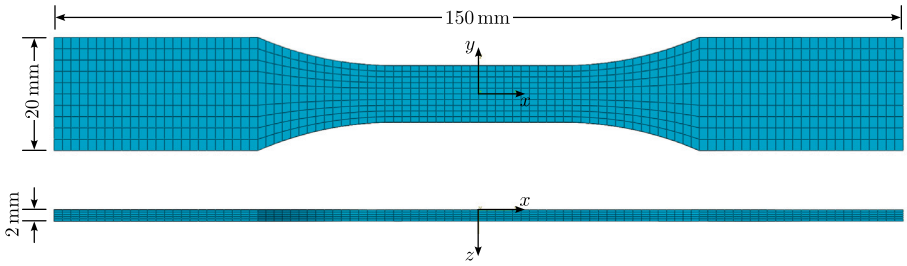

Fig. 5. Mesh of tensile specimen for statistical analysis and structural simulation with 4455 elements.

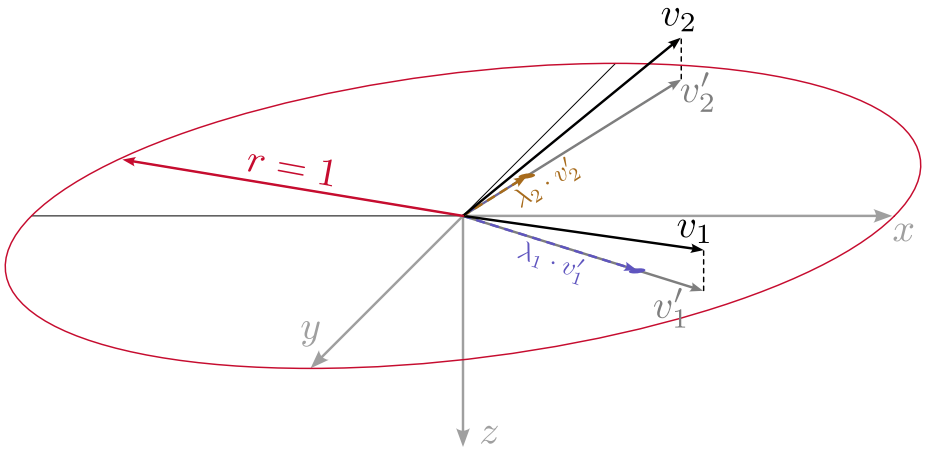

Fig. 6. Illustration of the projection scheme to visualize the orientation state of an element, where $\boldsymbol{v}_1$ and $\boldsymbol{v}_2$ are the first and second principal directions, $\boldsymbol{v}_1'$ and $\boldsymbol{v}_2'$ are their projection into the global x-y-plane and λ_1 and λ_2 are the corresponding eigenvalues, respectively.

specimen position and each injection molding distribution assumption. The set of orientation realizations is indicated with $\{\hat{\boldsymbol{z}}_k^{\text{ori}}\}$, where $k \in [0, 19]$.

To illustrate the distribution of drawn orientations for each group of injection molding simulations, a novel graphical representation is used. For this, the orientation state of each structural element of all $n = 20$ simulations is collected in one polar diagram.

For each structural element, the first and second principal orientation directions, i.e., $\boldsymbol{v}_1$ and $\boldsymbol{v}_2$, are first projected into the global x-y-plane, since the z-direction is of minor importance for the given process. The projected vector is then scaled by its eigenvalue λ_1 or λ_2, respectively. The resulting point to which the vector points is plotted in the polar diagram. This is illustrated in Fig. 6. The interpretation is that a point that is in the vicinity of the unit circle indicates strongly aligned fibers in that direction, because both the angle between the orientation vector $\boldsymbol{v}_1$ and the x-y-plane must be small, and the first eigenvalue must be close to one, i.e., $\lambda_1 \approx 1$. Only this combination results in a scaled projection close to the unit circle. Contrarily, a point that is close to the origin either indicates an orientation vector, which has a large out-of-plane component or a vanishing associated eigenvalue, or both, respectively.

The negative of an orientation vector represents the same orientation, i.e., $\boldsymbol{v}_i$ and $-\boldsymbol{v}_i$ are the same orientation in a material sense. This symmetry with respect to the origin of orientation vectors can be used to restrict the orientation vector illustration to two instead of four possible quadrants. In the given study, the first principal orientation is restricted to the first and fourth quadrants, which requires to first flip all orientation vectors, which point within the other two quadrants. The second principal direction is limited to the first and second quadrants. This gives a more structured overview of the orientation distribution.

Lastly, the cumulative orientation distribution projection can be evaluated statistically. For this, the mean orientation angle is calculated with respect to the global x-axis for the first principal direction or with respect to the global y-axis for the second principal direction. The mean angle is the angle of a vector to the corresponding global coordinate axis, which minimizes the sum of squared angles to all projected orientations. Based on this vector, a standard deviation in angle differences can be computed, which is representative of the orientation scatter within the projection plane. Likewise, the mean and standard deviation of the scaled length (radial distance) may be computed, which is representative for the degree of fiber concentration.

(b) Conditional distribution of elastic parameters

Based on a previous study by Rohrmüller et al. [33], where elastic and damage parameters were fitted to experimental data for different orientation states for a set of SVEs, the statistical distribution of $\hat{\boldsymbol{Z}}^{\text{el}}$ can be evaluated. Now, for each drawn realization of the orientation state $\hat{\boldsymbol{z}}_k^{\text{ori}}$ from the previous section, a conditional distribution for the elastic parameters only for known orientation values can be calculated, which will be normally distributed as well, based on the assumptions made. This conditional distribution is calculated for each element of the structural simulation based on the corresponding orientation realization. The elastic SVE data over the orientation eigenvalues is illustrated in Fig. A.15, while the damage parameters are given in Fig. A.16 in Appendix A. The marginalized expectation value over the orientation triangle is given with the linear regression hyperplane.

Based on the conditional distributions $\hat{\boldsymbol{Z}}^{\text{el}} \mid \lambda_i = f(\hat{\boldsymbol{z}}_k^{\text{ori}})$, realizations for the elastic parameters are drawn, which will be assigned to the element's material definition in a subsequent stage. The conditional distribution is only affected by the known values of the orientation eigenvalues λ_1 and λ_2, while the orientation eigenvectors $\boldsymbol{v}_i$ do not have an influence on the elastic parameters themselves. Still, it is the orientation eigenvectors that determine the material orientation for the assumed orthogonal material symmetry. Consequently, each element of the structural simulation has a unique element orientation, i.e., the orientation eigenvectors, and unique material parameters which are based on the orientation eigenvalues.

(c) Conditional distribution of damage parameters

In a last step, based on the drawn orientation and elastic parameters, the conditional distributions for the damage parameters are calculated and realizations are drawn. This is identical to the previous step.

The reason to draw the elastic and damage parameters in subsequent steps and not at once is that the distribution data for both sets of parameters are different. More specifically, the distribution data for the damage parameters is a subset of the distribution data for the elastic parameters.

3.5. Constitutive model

The constitutive or material model is a linear elastic model with orthotropic symmetry. The model is extended for failure, which is based on an elliptic failure criterion in stress space. Since `Abaqus/Standard` does not natively provide this combination, it was implemented in a `UMAT`.

The stress–strain relation is

$$\boldsymbol{\sigma} = \mathbb{C} : \boldsymbol{\varepsilon}, \tag{21}$$

where $\boldsymbol{\sigma}$ and $\boldsymbol{\varepsilon}$ are the stress and infinitesimal strain tensors, while $\mathbb{C}$ is the elasticity or stiffness tensor, respectively. In the non-normalized Voigt notation, as it is used in the `UMAT` environment within `Abaqus/Standard`, the orthotropic elasticity tensor is defined through

$$\mathbb{C} = \begin{bmatrix} C_{11} & C_{12} & C_{13} & 0 & 0 & 0 \\ C_{21} & C_{22} & C_{23} & 0 & 0 & 0 \\ C_{31} & C_{22} & C_{33} & 0 & 0 & 0 \\ 0 & 0 & 0 & C_{44} & 0 & 0 \\ 0 & 0 & 0 & 0 & C_{55} & 0 \\ 0 & 0 & 0 & 0 & 0 & C_{66} \end{bmatrix}, \tag{22}$$

where

$$C_{11} = (1 - \nu_{23}\nu_{32})\frac{E_1}{D}, \tag{23}$$

$$C_{12} = (\nu_{21} + \nu_{23}\nu_{31})\frac{E_1}{D}, \tag{24}$$

$$C_{13} = (\nu_{31} + \nu_{32}\nu_{21})\frac{E_1}{D}, \tag{25}$$

$$C_{21} = (\nu_{12} + \nu_{13}\nu_{32})\frac{E_2}{D}, \tag{26}$$

$$C_{22} = (1 - \nu_{13}\nu_{31})\frac{E_2}{D}, \tag{27}$$

$$C_{23} = (\nu_{32} + \nu_{31}\nu_{12})\frac{E_2}{D}, \tag{28}$$

$$C_{31} = (\nu_{13} + \nu_{12}\nu_{23})\frac{E_3}{D}, \tag{29}$$

$$C_{32} = (\nu_{23} + \nu_{21}\nu_{13})\frac{E_3}{D}, \tag{30}$$

$$C_{33} = (1 - \nu_{12}\nu_{21})\frac{E_3}{D}, \tag{31}$$

$$C_{44} = G_{12} \tag{32}$$

$$C_{55} = G_{13} \tag{33}$$

$$C_{66} = G_{23}, \tag{34}$$

and

$$D = 1 - \nu_{12}\nu_{21} - \nu_{13}\nu_{31} - \nu_{23}\nu_{32} - 2\nu_{12}\nu_{23}\nu_{31}. \tag{35}$$

In the orthotropic case, only three Poisson's ratios are independent, since

$$\nu_{21} = \nu_{12}\frac{E_2}{E_1}, \tag{36}$$

$$\nu_{31} = \nu_{13}\frac{E_3}{E_1}, \tag{37}$$

$$\nu_{32} = \nu_{23}\frac{E_3}{E_2}. \tag{38}$$

Besides the nine independent material parameters, which are $\{E_1, E_2, E_3, G_{12}, G_{13}, G_{23}, \nu_{12}, \nu_{13}, \nu_{23}\}$, the three principal directions of orthotropic symmetry need to be known, only in which the orthotropic elastic tensor takes the form in Eq. (22). This material orientation coincides with the orientation tensor eigenvectors $\boldsymbol{v}_i$.

For the failure criterion, the `UMAT` evaluates at each iteration for each integration point whether the stress state lies within the ellipsoid spanned by the half-axis defined through the damage parameters of the Hill yield criterion. Failure is assumed when

$$\left(\frac{\sigma_{11}}{\sigma^0 H_{11}}\right)^2 + \left(\frac{\sigma_{22}}{\sigma^0 H_{22}}\right)^2 + \left(\frac{\sigma_{33}}{\sigma^0 H_{33}}\right)^2 + \left(\frac{\sigma_{12}}{\sigma^0 H_{12}}\right)^2 + \left(\frac{\sigma_{13}}{\sigma^0 H_{13}}\right)^2 + \left(\frac{\sigma_{23}}{\sigma^0 H_{23}}\right)^2 > 1, \tag{39}$$

with a reference yield stress $\sigma^0 = 300$ MPa.

4. Results

4.1. Distribution of orientations for different process simulation distributions

The illustration of the drawn orientations across a specimen position and for a given injection molding distribution is given in Table 1. The different columns represent each specimen position, i.e., SP1-90°, SP2-0°, SP3-90° and SP4-0°. The different rows represent the different assumptions on how the injection molding results are distributed, that is, equally likely (uni), normally distributed with the parameter range being covered by $3\,\sigma$, and normally distributed with the parameter range being covered by $6\,\sigma$. This indicates that the expected scatter should decrease from top to bottom. The exact numerical values for the mean angle and radius and their standard deviation are given in Table B.3 in Appendix B.

Despite using different seeds for each injection molding distribution, the orientation patterns are almost indistinguishable across one specimen position for different distributions. Arguably, the patterns are more defined with clearer agglomerations for the $6\,\sigma$-assumption. The numerical values of mean and standard deviation for the orientation state are also almost identical for each specimen position.

SP1-90° has an agglomerated orientation state of the first principal direction in alignment with the global x-direction with a radial distance of $r_1 = 0.65 \pm 0.1$. Besides the central agglomeration, the remaining angular distribution appears to be equally distributed across the half-circle, with a slight second agglomeration near the angular boundaries of ±90°. The angular scatter is given with $\sphericalangle \boldsymbol{v}_1, \boldsymbol{x} = 1.8° \pm 31.9°$. The second principal direction has a radial distance of $r_2 = 0.29 \pm 0.08$, indicating a weaker alignment of fibers towards the global y-direction. Contrary to the first principal direction, the orientations seem to be strongly concentrated towards the global y-direction, but also towards the global x-direction, albeit to a lesser extent. The second angular position is given with $\sphericalangle \boldsymbol{v}_2, \boldsymbol{y} = 0.0° \pm 31.8°$, so the scatter between both principal directions is almost identical.

SP2-0° has a more concentrated orientation state than SP1-90°. The first principal direction has a radial distance of the scaled projection of $r_1 = 0.8 \pm 0.07$, which is larger than the previously discussed specimen position. Moreover, the angular position is $\sphericalangle \boldsymbol{v}_1, \boldsymbol{x} = 2.3° \pm 9.7°$, which is a vastly reduced scatter range, but also well aligned with the global x-direction. The scaled projection of the second principal direction has a smaller radial distance of $r_2 = 0.18 \pm 0.07$ and again a much smaller angular scatter with also $\sphericalangle \boldsymbol{v}_2, \boldsymbol{y} = 2.3° \pm 9.7°$. The second agglomerations at ±90° as seen in the previous specimen position do not occur for SP2-0°.

SP3-90° reveals a statistically more aligned microstructure than its orientation equivalent SP1-90°. The first principal direction has a projected radial distance of $r_1 = 0.76 \pm 0.08$, which is higher than SP1-90° but slightly lower than SP2-0°. The angular position for the

Table 1
Graphical representation of the orientation states for the different specimen positions and the different distributions of injection molding results. The blue dots indicate the scaled direction of the principal direction with the largest eigenvalue (restricted to the first and fourth quadrant), while the orange dots indicate the scaled direction of the principal direction with the second-largest eigenvalue (restricted to the first and second quadrant).

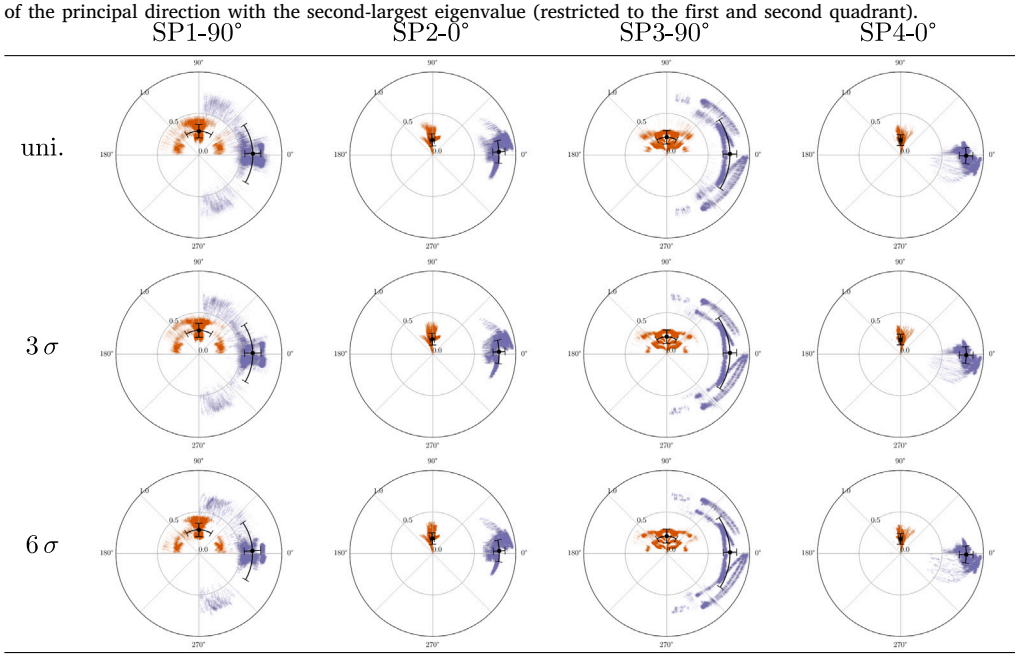

first projected direction is $\sphericalangle \boldsymbol{v}_1, \boldsymbol{x} = 1.0° \pm 33.4°$, which once more is a relatively large angular scatter band. Despite having almost identical angular statistics with SP1-90°, the visual interpretation is different. While SP1-90° has a major concentration of orientation states around the global x-direction, SP3-90° shows pronounced orientation bands that are more evenly distributed across a wider angle range. Another difference is that SP3-90° has fewer first principal direction pointing towards the global y-axis. The second principal direction shows a radial position of $r_2 = 0.21 \pm 0.08$, which supports the more prominent first principal direction. The angular position is given with $\sphericalangle \boldsymbol{v}_2, \boldsymbol{y} = 0.0° \pm 33.3°$, which numerically is very similar to the orientation equivalent SP1-90°. Visually, the concentrated patches towards the global x-axis are less pronounced, though.

The last specimen position SP4-0° reveals strong similarities in the orientation state with SP2-0°. Both principal orientation directions are strongly agglomerated around their reference global axes. The radial distribution of the first principal direction is $r_1 = 0.79 \pm 0.08$, which is just short of the values for SP2-0°. The angular position is $\sphericalangle \boldsymbol{v}_1, \boldsymbol{x} = -0.8° \pm 7.2°$, making this specimen position the only one for which the average first principal direction points into the fourth quadrant, albeit to a negligible degree. The angular scatter of $\pm 7.2°$ is the lowest of all four specimen positions for the first principal direction, indicating strongly aligned fibers, which is supported by the rather large mean value of r_1. The second principal direction has a radial position of $r_2 = 0.18 \pm 0.06$, which is again very similar to the orientation equivalent SP2-0°. The angular distribution is $\sphericalangle \boldsymbol{v}_2, \boldsymbol{y} = 0.0° \pm 7.2°$, giving a slightly reduced scatter compared to the other zero degree specimen and again the lowest second angular scatter overall.

4.2. Distribution of input material parameters for different process simulation distributions

Based on the drawn orientation states for each specimen position, each injection molding distribution assumption, and each of the $n = 20$ simulation runs, the material parameters were drawn from the conditional distribution, as explained in the methodology. The elastic parameters of each structural element for the $n = 20$ simulations for each specimen position and injection molding distribution assumption are evaluated in histograms, which are summarized in Figs. C.17, C.18 and C.19 in Appendix C.

Without discussing all the 9 elastic parameters for each of the 4 specimen positions individually, it is evident that the distribution of the drawn material parameters for different injection molding parameter distributions is indifferent for every specimen position. Based on the assumptions made in the methodology, the stiffness parameters E_i and G_{ij} are visibly log-normally distributed, while the Poisson's ratios ν_{ij} are clearly normally distributed.

4.3. Distribution of effective material parameters for different process simulation distributions for orientation dependent material parameters

The results of the numerical tensile test and the evaluation of the distribution for the effective Young's modulus in the testing direction are given in Figs. 7, 8, 9 and 10. The left plot visualizes the stress–strain response for the three different assumptions on the distribution of the injection molding parameters. The right plot gives the cumulative distribution of the effective Young's modulus in test direction, which was evaluated between the strain values of $\varepsilon_1 = 0.05\%$ and $\varepsilon_2 = 0.25\%$. The experimental results are discussed in the original contribution (Rohrmüller et al. [35]), but they are not directly related because the specimen thickness is increased in the experiment. Nevertheless, they are included for reference cases.

Throughout all specimen positions, the stress–strain curves are hard to distinguish from one another for different injection molding parameter distributions. The corresponding values for the Young's modulus between the distribution assumptions are similar, and also the mean stress/strain values at failure do not vary significantly.

The results for SP1-90° are visualized in Fig. 7. The comparison with the experimental stress–strain curves shows a good agreement with real data, albeit the experimental data suffering from larger scatter when the strain increases. The cumulative distribution of the Young's modulus is shifted slightly to the left for all numerical cases, and the width of the CDF is in general more narrow. Based on the fitted log-normal CDF function, the parameters reveal that the mean value of the

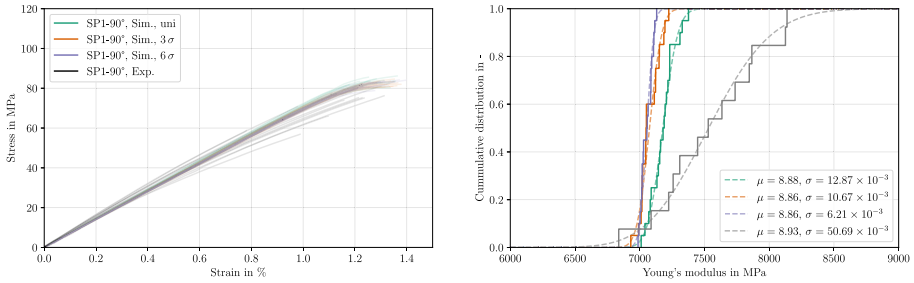

Fig. 7. Simulated and experimental tensile tests and derived cumulative distribution function (CDF) of Young's modulus for SP1-90°. The parameters in the right plot are the best fit parameters for a log-normal distribution of the CDF.

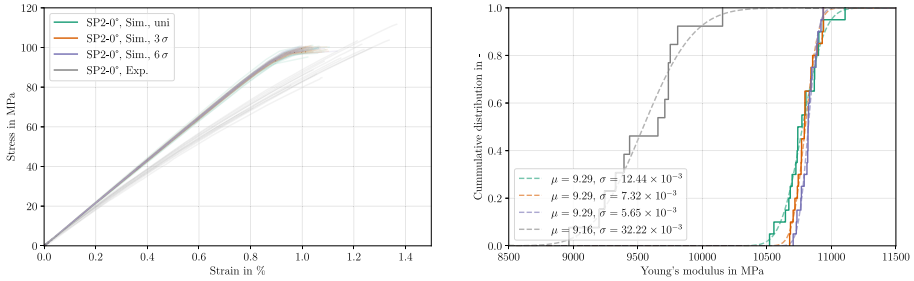

Fig. 8. Simulated and experimental tensile tests and derived cumulative distribution function (CDF) of Young's modulus for SP2-0°. The parameters in the right plot are the best fit parameters for a log-normal distribution of the CDF.

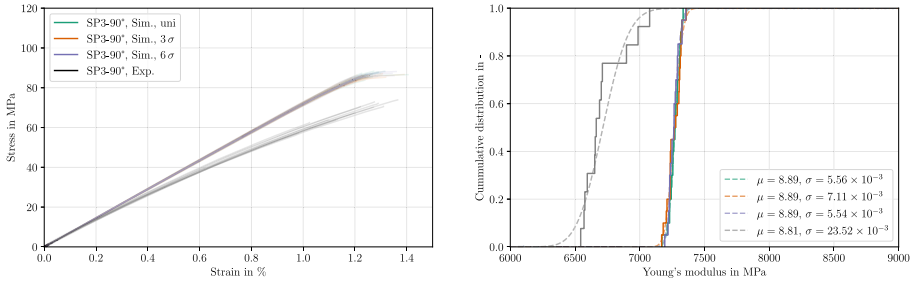

Fig. 9. Simulated and experimental tensile tests and derived cumulative distribution function (CDF) of Young's modulus for SP3-90°. The parameters in the right plot are the best fit parameters for a log-normal distribution of the CDF.

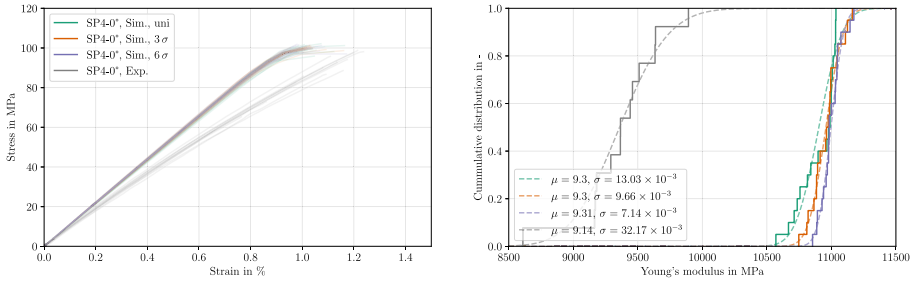

Fig. 10. Simulated and experimental tensile tests and derived cumulative distribution function (CDF) of Young's modulus for SP4-0°. The parameters in the right plot are the best fit parameters for a log-normal distribution of the CDF.

Young's modulus for different injection molding parameter assumptions is nearly identical with $\mu = 8.86$ for the equally likely assumption and $\mu = 8.86$ for the remaining two assumptions, giving a mean Young's modulus of 7186 MPa and 7044 MPa, respectively. The scatter band shows a larger variance, though. The equally likely assumption (uni.) shows the widest distribution with $\sigma = 12.87 \times 10^{-3}$ for the fitted log-normal CDF. A slightly more narrow distribution is given with the $3\,\sigma$-assumption with $\sigma = 10.67 \times 10^{-3}$, and the $6\,\sigma$-assumption gives a significantly more narrow distribution with a fitted parameter of $\sigma = 6.21 \times 10^{-3}$.

For the second specimen position SP2-0° in Fig. 8, the effective stress–strain response shows a stiffer material response as compared with the experimental result. Again, the visible scatter is small compared with real-world data. The CDF of the Young's modulus confirm a shifted mean Young's modulus to larger values for all injection molding parameter assumptions at identical $\mu = 9.29$, which translates to a mean Young's modulus of 10 829 MPa. As in the previous case, the width of the CDF, which is representative of the scatter tendency, follows a declining trend for more concentrated parameter distributions in the injection molding simulation. The largest scatter is observed for the

equally likely case with $\sigma = 12.44\times10^{-3}$ followed by the $3\,\sigma$-assumption with $\sigma = 7.32 \times 10^{-3}$ and the most narrow CDF is given with the $6\,\sigma$-assumption with a scatter parameter of $\sigma = 5.65 \times 10^{-3}$.

The other specimen perpendicular to the flow direction is SP3-90°, for which the numerical results are given in Fig. 9. Just as in the previously discussed case, the stress–strain data show a stiffer response for the numerical tests compared to the real-world data. This time, the scatter band of the experimental stress–strain data is also reduced. When the CDF of the Young's moduli are compared, a different picture emerges compared to the previous results. Again, the mean of the numerical results is larger than the experimental result, with an identical mean value of $\mu = 8.89$, which translates to a mean effective Young's modulus of 7259 MPa. For this specimen, the CDF of the numerical tensile tests for different injection molding parameter assumptions is in general more narrow, and the monotonic trend is not continued. The CDF widths are given with $\sigma = 5.56 \times 10^{-3}$, $\sigma = 7.11 \times 10^{-3}$ and $\sigma = 5.54 \times 10^{-3}$ for the uni., $3\,\sigma$ and $6\,\sigma$-assumption, respectively.

The results for the remaining specimen SP4-0° are given in Fig. 10. The results are qualitatively and quantitatively similar to the direction equivalent SP2-0°. The numerical results give a stiffer stress–strain response in comparison to the experimental data, and the scatter is visibly smaller. For the CDF of the effective Young's modulus, the same picture emerges as before. All numerical investigations have a higher mean stiffness compared to the real-world data with a fitted log-normal parameter of $\mu = 9.3$, which is a mean Young's modulus of 10 938 MPa, slightly above SP2-0°. The width of the logarithmic CDF again follows a monotonic trend with respect to the injection molding parameter assumptions. The highest variability is measured for the case in which the injection molding simulations are equally likely, with a parameter of $\sigma = 13.03 \times 10^{-3}$. A lower scatter band is observed for the $3\,\sigma$-assumption with $\sigma = 7.14 \times 10^{-3}$ and a further reduction is given for the $6\,\sigma$-assumption with $\sigma = 7.14 \times 10^{-3}$

4.4. Distribution of effective material parameters for different process simulation distributions with deterministic material parameters

In the previous section, both the spatial correlation of the orientation state per specimen position and the material scatter across the orientation triangle were considered. In the following section, the functional relation between the orientation state and material input parameters is still considered in an average sense, but the scatter is disabled, which coincides with the assumption that for a given orientation state the material properties are deterministic. Nevertheless, the material properties may still vary between different orientation states. This is a special case of the introduced methodology, for which the material parameters are determined based on the conditional mean $\boldsymbol{\mu}_{1|2}$ in Eq. (9) only. This is equal to the linear regression across the orientation triangle, which is also the best predictor for the material parameters. To avoid excessive repetition in the discussion, this is only performed on SP1-90° and SP2-0°.

The results for both cases are given in Figs. 11 and 12. The left plots show the stress–strain response, while the right plots show the CDF of the Young's modulus for different injection molding parameter distribution assumptions. It is generally visible that the onset of failure is postponed to significantly higher stresses and strains.

The results of the specimens that were tested in the direction perpendicular to the flow SP1-90 are given in Fig. 11. Besides the already mentioned increase in failure stress/strain, a contrast to the results of the previous section emerges for the CDF of the Young's modulus. A slight reduction in the mean stiffness is seen for all distribution assumptions, with an average stiffness of 6856 MPa. Moreover, the scatter patterns are different. For all cases, the scatter parameter σ is reduced compared to the previous section, where the modeled material uncertainty was considered. The reduction of the scatter parameter is small for the equally likely and the $3\,\sigma$-assumption with $\sigma = 11.04\times10^{-3}$ and $\sigma = 10.03 \times 10^{-3}$, respectively. Contrary, the CDF width for the $6\,\sigma$-assumption is reduced more significantly to $\sigma = 3.93 \times 10^{-3}$.

Similarly, the tensile specimen in flow direction SP2-0 shows an increase in failure strain/stress. While the injection molding parameter distributions, which are normally distributed, show a sudden failure, the equally likely assumption has a zone of progressive damage accumulation. The distributions of the Young's modulus continue the trend of the 90° specimen, just more pronounced. The mean stiffness is reduced to 10 404 MPa, while the scatter is also reduced. For the equally likely parameter assumption, the reduction in the scatter parameter is quite small, with $\sigma = 11.61\times10^{-3}$. The relative reduction then increases for the $3\,\sigma$-assumption to $\sigma = 4.83 \times 10^{-3}$ and even further for the $6\,\sigma$-assumption to $\sigma = 2.56 \times 10^{-3}$, which is less than half the scatter parameter of the previous section with considered material scattering.

4.5. Distribution of effective material parameters for different process simulation distributions with invariant material parameters

To investigate to what extent the variability of the effective material parameters, which in our case is the effective stiffness property, can be attributed to the total variability of the constitutive parameters, i.e., $\{E_1, E_2, \dots\}$, the numeric investigation is repeated for constant input parameters over the specimen. Therefore, instead of drawing input material properties based on the conditional distribution for drawn orientations, the mean input material property is assigned to each structural element, no matter its orientation state. Thereby, the degree of orientation through the magnitudes of λ_1 and λ_2 do not affect the input material parameters, while the orientation eigenvalues still determine the orthogonal orientation distribution. This is an extreme case in which the input material parameters are treated as independent of the microstructure. Again, to avoid excessive repetition in the discussion, this is only performed on SP1-90° and SP2-0°.

The results showing the stress–strain response and the CDF of the Young's modulus in test direction are given in Figs. 13 and 14. To allow for a better comparison, the results of the previous section in which orientational and material scatter were considered are also plotted in the figures. In general, the strain and stress at failure are excessively larger compared to the previous result, while the effects on the CDF of the Young's modulus need to be treated separately for the different load directions.

The first specimen position of SP1-90° is given in Fig. 13. The effective Young's modulus are in a similar range compared to the results of the previous section, albeit slightly shifted to lower effective stiffness values, with a mean stiffness of around 6815 MPa. While the CDF width is increased for the equally likely injection molding parameter assumption with $\sigma = 15.12\times10^{-3}$, the other two distribution assumptions show a reduction of the scatter parameter σ to half its previous value, with $\sigma = 5.73 \times 10^{-3}$ and $\sigma = 3.69 \times 10^{-3}$ for the $3\,\sigma$ and $6\,\sigma$-assumptions, respectively.

A different picture emerges for the tensile test in the flow direction of SP2-0° in Fig. 14. The CDF indicates that for all distribution assumptions the effective stiffness is vastly reduced to a mean stiffness of 9136 MPa in comparison to 10 829 MPa of the section in which the full parameter distribution was considered. Moreover, the scatter or width of the CDF is approaching a vanishing value while still following a trend of decreasing scatter for a more concentrated parameter distribution in the injection molding simulation. The scatter parameters are given with $\sigma = 51.83 \times 10^{-3}$, $\sigma = 1.04 \times 10^{-3}$ and $\sigma = 0.39 \times 10^{-3}$ for the equally likely, $3\,\sigma$ and $6\,\sigma$-assumptions, respectively.

4.6. Overview of results

To summarize the results, the fitted parameters of the Young's modulus CDF for each considered injection molding parameter assumption and the individual numerical studies are given in Table 2. Here, only the first two specimen positions SP1-90 and SP2-0 are considered representative for a tensile specimen perpendicular and in flow direction, respectively.

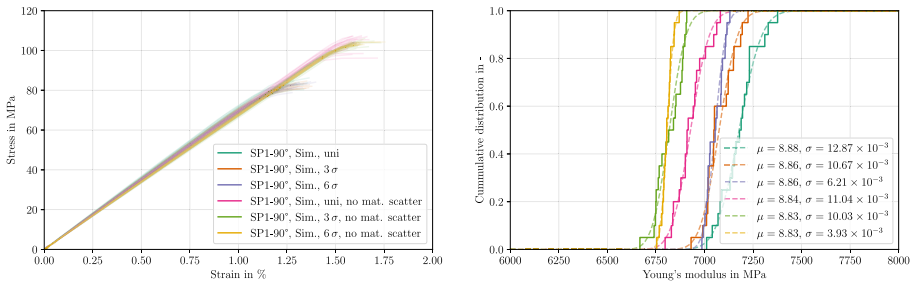

Fig. 11. Simulated and experimental tensile tests and derived cumulative distribution function (CDF) of Young's modulus for SP1-90° for orientation input material parameters with disabled scattering. The parameters in the right plot are the best fit parameters for a log-normal distribution of the CDF.

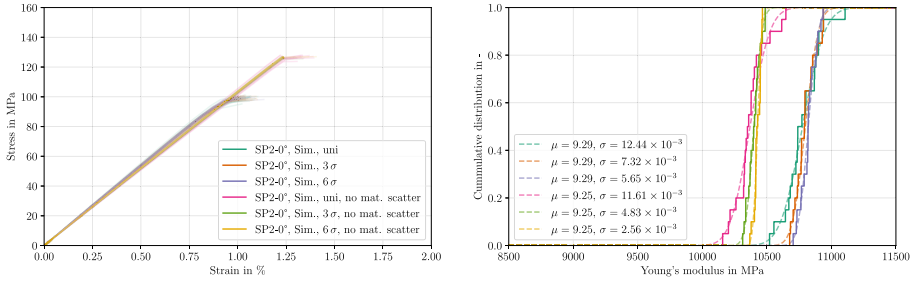

Fig. 12. Simulated and experimental tensile tests and derived cumulative distribution function (CDF) of Young's modulus for SP2-0° for orientation input material parameters with disabled scattering. The parameters in the right plot are the best fit parameters for a log-normal distribution of the CDF.

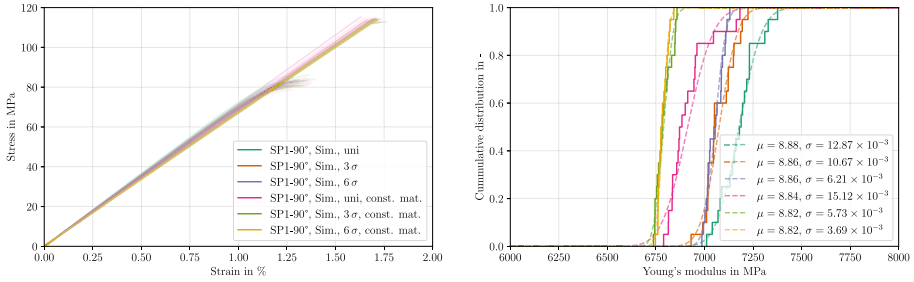

Fig. 13. Simulated and experimental tensile tests and derived cumulative distribution function (CDF) of Young's modulus for SP1-90° for orientation invariant input material parameters. The parameters in the right plot are the best fit parameters for a log-normal distribution of the CDF.

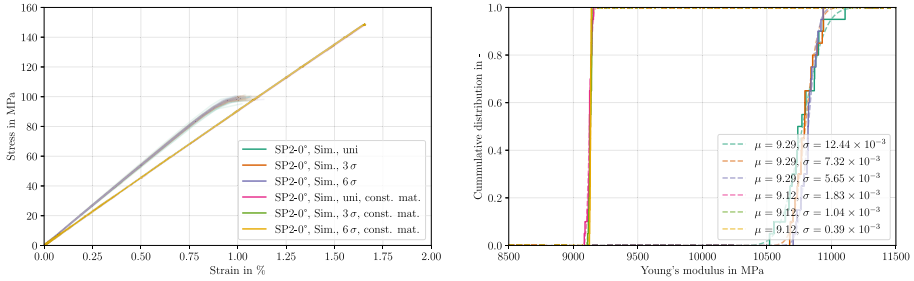

Fig. 14. Simulated and experimental tensile tests and derived cumulative distribution function (CDF) of Young's modulus for SP2-0° for orientation invariant input material parameters. The parameters in the right plot are the best fit parameters for a log-normal distribution of the CDF.

5. Discussion

The goal of the ongoing research was to present and investigate a methodology to numerically assess uncertainties and the propagation of uncertainties within injection-molded FRPs. The research question is concerned with the sources of uncertainties and their individual contribution to the scattering of effective properties, such as the effective Young's modulus of the composite. The uncertainties were reduced to originate from two different sources. One source is the uncertainty of the microstructure, which is caused by varying injection molding process parameters and which expresses itself in varying local orientation states. Other microstructural properties, such as fiber length distributions or varying fiber volume content, were ignored. The other source of uncertainty is caused by material scatter within a given orientation state.

The methodology is based on assuming that the orientation state throughout a structure can be described by a random vector, which includes the 5 independent components of the orientation tensor of second order for each FE element in the given geometry of interest. The distribution of this random vector is computed by evaluating the results of multiple injection molding simulations for varying input parameters. To investigate how the set of injection molding input parameters influences the effective properties of the composite, different assumptions were made on the distribution of the input parameters. These included

Table 2
Fitted logarithmic CDF parameters μ and σ for the individual results of the Young's modulus distribution for different injection molding parameter assumptions.

Injection mold. assumption:		uni.		3σ		6σ	
		μ	$\sigma \times 10^3$	μ	$\sigma \times 10^3$	μ	$\sigma \times 10^3$
Full distribution	SP1-90°	8.88	12.87	8.86	10.67	8.86	6.21
	SP2-0°	9.29	12.44	9.29	7.32	9.29	5.65
Disabled mat. scatter	SP1-90°	8.84	11.04	8.83	10.03	8.83	3.93
	SP2-0°	9.25	11.61	9.25	4.83	9.25	2.56
Const. mat. parameters	SP1-90°	8.84	15.12	8.82	5.73	8.82	3.69
	SP2-0°	9.12	1.83	9.12	1.04	9.12	0.39

the assumption that each input parameter may take on any value within a given range with equal probability or that the input parameters are normally distributed, so that half the range of valid input parameters is covered by 3σ or 6σ of a normal distribution, respectively. The expected outcome is that the orientation states across the structure should have a more pronounced scatter, i.e., larger uncertainty, the less the input parameters of the injection molding simulation are concentrated. Hence, the equally likely assumption should cause the greatest scatter of orientation states, and the 6σ-assumption should cause the least scatter, which may or may not be visible in the scatter of the effective properties of the composite. The material scatter was considered through a joint distribution with the orientation concentration, i.e., the orientation eigenvalues λ_1 and λ_2, which were computed from the results of previous SVE studies.

Although visually and statistically only small differences in the cumulative orientation state can be seen for different distribution assumptions of the injection molding parameters, an effect is clearly visible when the CDF of the effective modulus of elasticity and the parameters of the fitted lognormal CDF are compared (representative in Table 2). When orientational scatter and material scatter are considered, i.e., the *full distribution*, the width of the CDF monotonically decreases for more concentrated injection molding input parameters. This can only be explained by the trend of lower scattering in the input parameters also being reflected in the orientation state, giving reason to believe that the visual representations are not misleading in the perceived increased orientation concentration patterns. Moreover, when the scatter of the structural material parameter is disabled, different patterns between the distribution assumptions are evident. While for the equally likely case, the scatter parameter is only slightly reduced when the material parameters do not scatter, a significant reduction was visible for the 6σ-assumption. This is a clear indication that the different sources of scattering affect each other in a nonlinear fashion. It appears as if a more pronounced orientation scattering masks the material scattering in the investigated case, whereby the material scattering has hardly any effect on the effective stiffness. If the orientation states now occur in a more sorted manner, the influence of the uncertainties within the material parameters plays a significant role on the effective modulus of elasticity.

The study also showed clear differences in the sensitivity of the scattering behavior between the sample orientations. The scattering behavior of the samples perpendicular to the flow direction is generally greater, although the differences between the individual assumptions were smaller. This is most likely due to the fact that the position of the sample causes an increased variability of the flow properties along the geometry, which inevitably results in a higher scattering behavior. Therefore, switching off or changing individual sources of uncertainty is still at least partially compensated by the intrinsic scattering behavior of the orientation state.

The above argumentation shows that the causes of the scattering of effective parameters cannot be considered individually, and that a superposition does not appear to be sufficient. On the contrary, they must be considered as mutually influencing variables. This also means that an additional source of uncertainty does not necessarily have to be reflected in the effective behavior, as it can be dampened by other sources of uncertainty. Additionally, removing a source of uncertainty does also not necessarily reduce the effective scatter, as was seen in the study of keeping the material parameter constant no matter the orientation state. Only the individual activation and deactivation of sources of uncertainty, which is much easier in the numerical experiment, makes it possible to better assess the influences of the individual causes in the overall context.

In the presented case study, only a single sample geometry and a relatively simple injection molding structure in the form of a plate were examined. It is well known, especially for injection-molded parts, that a shell-core effect arises due to inhomogeneous flow properties along the height of the plate. The influence of the shell-core effect on the effective properties is linked to the proportion of the various phases, which in turn depends on the flow behavior and the geometry [45]. The proposed methodology is formulated generically, as the process simulation conducted in the initial step is interchangeably arbitrary. As long as the model of this process simulation yields valid results, such as predicting the orientation differences between the shell and core, these properties will be statistically represented in the subsequent structural simulation for a sufficient mesh resolution. Consequently, the methodology can also be individually extended to other microstructural effects, such as fiber length distribution.

A methodological bottleneck is represented by the quadratically increasing memory requirements associated with meshing and the resulting covariance matrix. In the proposed version of the methodology, the spatial correlation for the orientation state is computed among all considered structural elements. Therefore, it was necessary to evaluate only individual test samples at a time and to coarsen the structural finite element mesh in comparison to the process simulation. An analysis of mesh sensitivity was not addressed. There exists a lower bound on element size determined by the choice of dimensions for the representative or statistical volume elements, from which the joint distribution of effective material parameters and the eigenvalues of the orientation state was established. If a finer level of meshing is desired or required beyond what is presented here, sufficient memory must be available. As an alternative, an advancement of the methodology could involve initially subdividing the considered geometry into subgeometries for which local correlations are calculated respectively. Considering the inequality $n^2 = (n_1 + n_2 + \cdots + n_k)^2 \geq n_1^2 + n_2^2 + \cdots + n_k^2$ with $n_i \in \mathbb{Z}$, the subdivision of a domain with n elements into k disjoint subdomains with corresponding element counts n_i could potentially lead to a drastic reduction in memory usage. Future studies should explore how to optimally partition the entire domain and to what extent overlapping between subdomains may be necessary.

In summary, the methodology presented provides first successful insights into the analysis of sources of uncertainty and their mutual influences on effective material properties. Many simplifying assumptions were made in this work, such as the unjustified distributions, which should be better justified in future studies. The underlying process simulation provided intrinsically little scattering behavior, which meant that the subsequent differences were smaller than initially expected. Nevertheless, clear trends were identified, which can be built upon in subsequent studies.

6. Conclusion

This research successfully establishes a framework for numerically assessing uncertainties and their propagation within injection-molded fiber-reinforced polymers. By focusing on two primary sources of uncertainty, i.e., microstructural variability due to injection molding parameters and material scatter, the study elucidates the complex interplay between these factors and their collective impact on the effective properties, particularly the Young's modulus of the composite.

Key findings indicate that while the variations in orientation states across the structure were less pronounced than anticipated, clear patterns emerged when analyzing the cumulative distribution functions

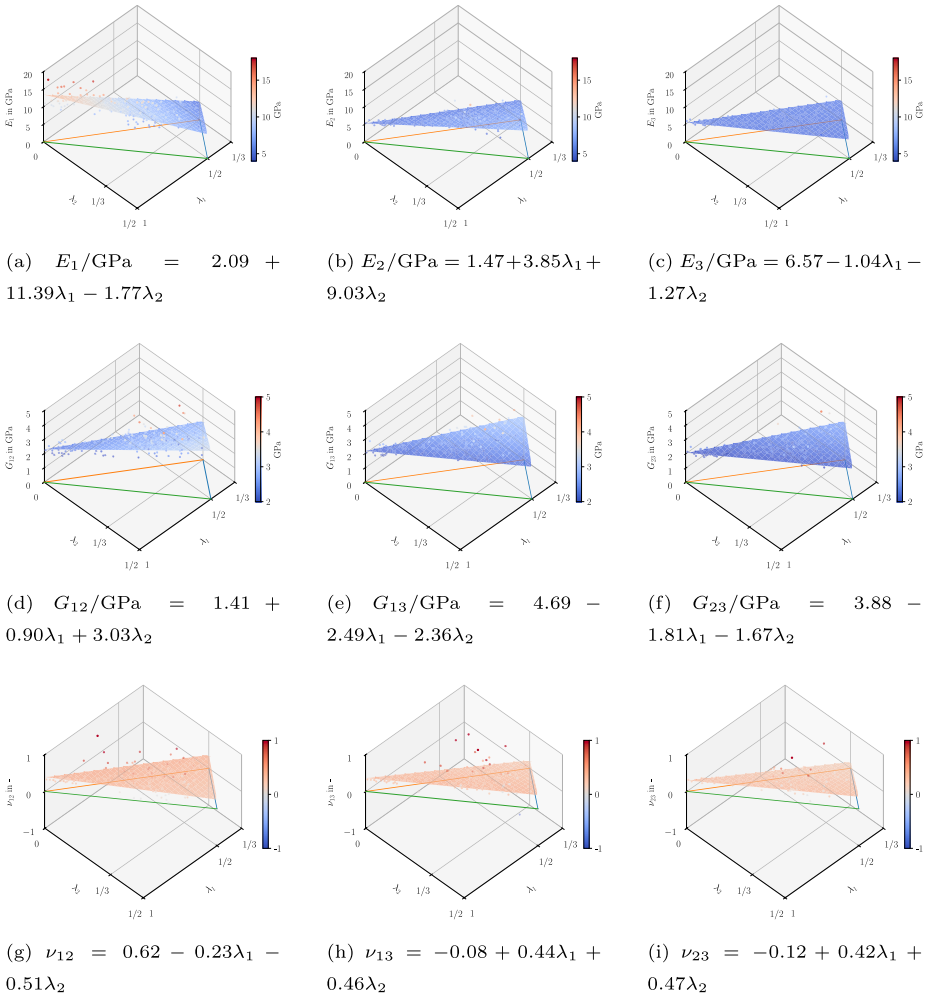

(a) $E_1/\mathrm{GPa} = 2.09 + 11.39\lambda_1 - 1.77\lambda_2$

(b) $E_2/\mathrm{GPa} = 1.47 + 3.85\lambda_1 + 9.03\lambda_2$

(c) $E_3/\mathrm{GPa} = 6.57 - 1.04\lambda_1 - 1.27\lambda_2$

(d) $G_{12}/\mathrm{GPa} = 1.41 + 0.90\lambda_1 + 3.03\lambda_2$

(e) $G_{13}/\mathrm{GPa} = 4.69 - 2.49\lambda_1 - 2.36\lambda_2$

(f) $G_{23}/\mathrm{GPa} = 3.88 - 1.81\lambda_1 - 1.67\lambda_2$

(g) $\nu_{12} = 0.62 - 0.23\lambda_1 - 0.51\lambda_2$

(h) $\nu_{13} = -0.08 + 0.44\lambda_1 + 0.46\lambda_2$

(i) $\nu_{23} = -0.12 + 0.42\lambda_1 + 0.47\lambda_2$

Fig. A.15. Distribution of individual material parameters of SVE study over orientation triangle, including expectation value, i.e., linear regression hyperplane, and hyperplane coefficients. The interpretation of the colored edges of the orientation triangle can be taken from Fig. 1. (For interpretation of the references to color in this figure legend, the reader is referred to the web version of this article.)

of the effective modulus of elasticity. The results demonstrate that more concentrated injection molding parameters lead to a reduction in the width of the CDF, but also demonstrate a non-linear relationship between orientation scatter and material scatter. This underscores the necessity of considering these uncertainties as interdependent rather than isolated factors.

Moreover, the sensitivity of scattering behavior varied with sample orientation, emphasizing the influence of geometry on flow properties and, consequently, on material performance. The study reveals that the effects of uncertainty sources can mask one another, indicating that eliminating a source of uncertainty does not straightforwardly reduce effective scatter. Thus, a nuanced understanding of the interactions between various uncertainties is crucial for accurately predicting the behavior of composite materials.

In conclusion, this work lays the groundwork for future investigations into the effects of uncertainties in FRPs, suggesting that more extensive parameter variations and refined distribution assumptions could yield deeper insights. The methodology developed here is a significant step towards comprehensively understanding the factors influencing effective material properties, paving the way for improved design and manufacturing processes in polymer composites.

CRediT authorship contribution statement

Nicolas Christ: Writing – original draft, Visualization, Validation, Software, Methodology, Investigation, Formal analysis, Data curation. **Florian Wittemann:** Writing – original draft, Investigation. **Benedikt Rohrmüller:** Investigation, Formal analysis. **Jörg Hohe:** Writing – review & editing, Writing – original draft, Supervision, Resources, Project administration. **Luise Kärger:** Funding acquisition. **Carla Beckmann:** Writing – review & editing, Supervision, Project administration, Funding acquisition.

Declaration of competing interest

The authors declare that they have no known competing financial interests or personal relationships that could have appeared to influence the work reported in this paper.

Acknowledgments

The present work has been funded by the Deutsche Forschungsgemeinschaft (DFG, German Research Foundation), Germany under Grant no. 464119659. The financial support is gratefully acknowledged.

Appendix A. SVE material parameter over orientation eigenvalues

See Figs. A.15 and A.16.

Appendix B. Drawn material orientation statistics

See Table B.3.

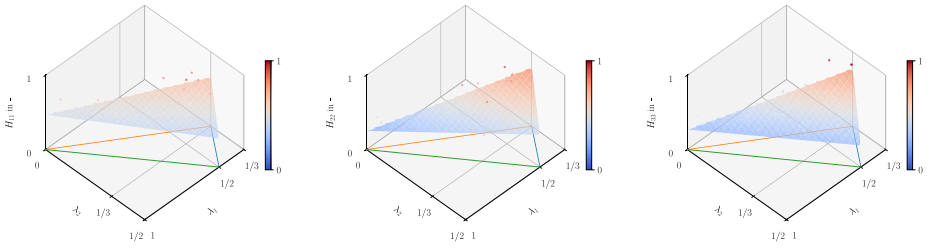

(a) $H_{11} = 1.22 - 0.75\lambda_1 - 0.92\lambda_2$ (b) $H_{22} = 1.51 - 1.25\lambda_1 - 0.89\lambda_2$ (c) $H_{33} = 1.76 - 1.49\lambda_1 - 1.45\lambda_2$

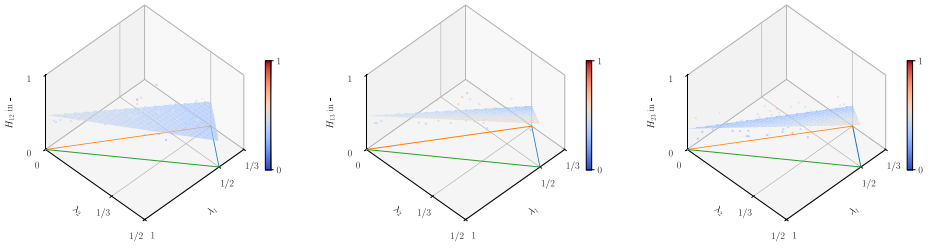

(d) $H_{12} = 0.31 + 0.15\lambda_1 - 0.07\lambda_2$ (e) $H_{13} = -0.35 + 0.80\lambda_1 + 1.06\lambda_2$ (f) $H_{23} = -0.30 + 0.58\lambda_1 + 1.15\lambda_2$

Fig. A.16. Distribution of individual material parameters of SVE study over orientation triangle, including expectation value, i.e., linear regression hyperplane, and hyperplane coefficients. The interpretation of the colored edges of the orientation triangle can be taken from Fig. 1. (For interpretation of the references to color in this figure legend, the reader is referred to the web version of this article.)

Table B.3
Mean (μ) and standard deviation (std.) of the radial and angular position of the projected and scaled orientations for different specimen positions and injection molding distribution assumptions.

		SP1-90°		SP2-0°		SP3-90°		SP4-0°	
		μ	std.	μ	std.	μ	std.	μ	std.
uni.	r_1	0.65	0.10	0.80	0.08	0.76	0.08	0.79	0.08
	r_2	0.29	0.08	0.18	0.07	0.21	0.08	0.18	0.06
	$\sphericalangle \boldsymbol{v}_1, \boldsymbol{x}$	1.5°	31.9°	2.7°	9.7°	0.8°	32.9°	−0.6°	7.0°
	$\sphericalangle \boldsymbol{v}_2, \boldsymbol{y}$	0.0°	31.8°	2.7°	9.8°	0.0°	32.9°	0.0°	6.9°
$3\,\sigma$	r_1	0.65	0.10	0.80	0.07	0.76	0.08	0.79	0.08
	r_2	0.29	0.08	0.18	0.07	0.21	0.08	0.18	0.06
	$\sphericalangle \boldsymbol{v}_1, \boldsymbol{x}$	1.2°	31.8°	2.1°	10.1°	1.2°	34.0°	−0.8°	7.3°
	$\sphericalangle \boldsymbol{v}_2, \boldsymbol{y}$	0.0°	31.7°	2.1°	10.1°	0.0°	33.9°	0.0°	7.2°
$6\,\sigma$	r_1	0.65	0.10	0.80	0.07	0.76	0.08	0.79	0.08
	r_2	0.28	0.08	0.18	0.07	0.21	0.08	0.17	0.06
	$\sphericalangle \boldsymbol{v}_1, \boldsymbol{x}$	2.7°	32.1°	2.1°	9.4°	1.0°	33.3°	−1.0°	7.3°
	$\sphericalangle \boldsymbol{v}_2, \boldsymbol{y}$	0.0°	31.9°	2.0°	9.4°	0.0°	33.2°	0.0°	7.4°

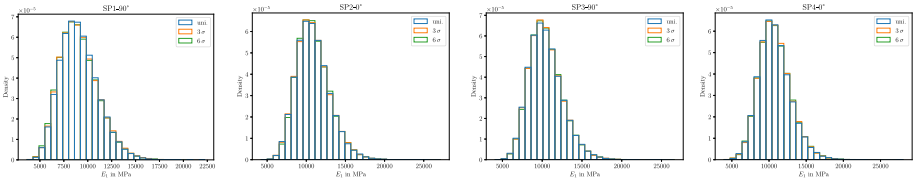

(a) SP1-90°, E_1 (b) SP2-0°, E_1 (c) SP3-90°, E_1 (d) SP4-0°, E_1

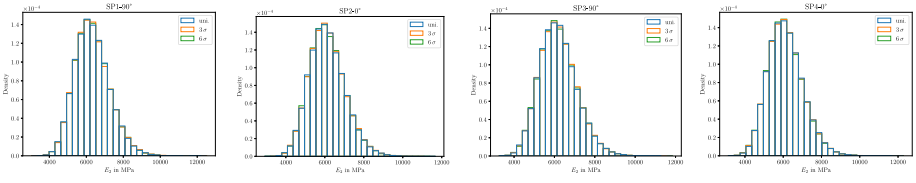

(e) SP1-90°, E_2 (f) SP2-0°, E_2 (g) SP3-90°, E_2 (h) SP4-0°, E_2

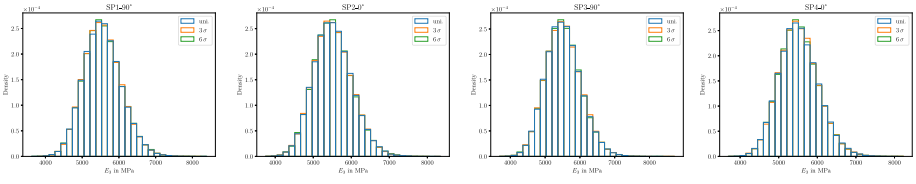

(i) SP1-90°, E_3 (j) SP2-0°, E_3 (k) SP3-90°, E_3 (l) SP4-0°, E_3

Fig. C.17. Drawn material parameters E_1, E_2 and E_3 across all structural elements and all simulated cases based on the conditional distribution of the orientation state for different specimen position and injection molding distribution assumptions.

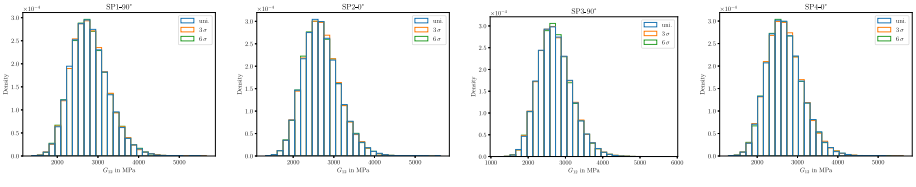

(a) SP1-90°, G_{12} (b) SP2-0°, G_{12} (c) SP3-90°, G_{12} (d) SP4-0°, G_{12}

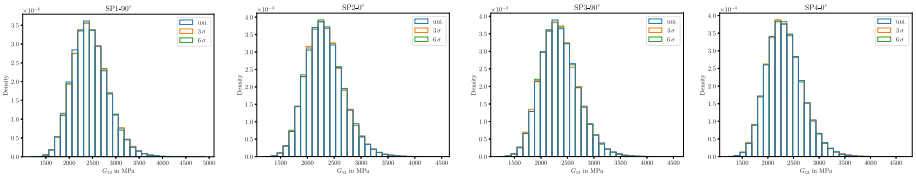

(e) SP1-90°, G_{13} (f) SP2-0°, G_{13} (g) SP3-90°, G_{13} (h) SP4-0°, G_{13}

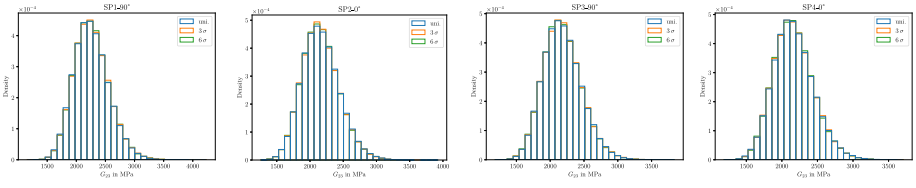

(i) SP1-90°, G_{23} (j) SP2-0°, G_{23} (k) SP3-90°, G_{23} (l) SP4-0°, G_{23}

Fig. C.18. Drawn material parameters G_{12}, G_{13} and G_{23} across all structural elements and all simulated cases based on the conditional distribution of the orientation state for different specimen position and injection molding distribution assumptions.

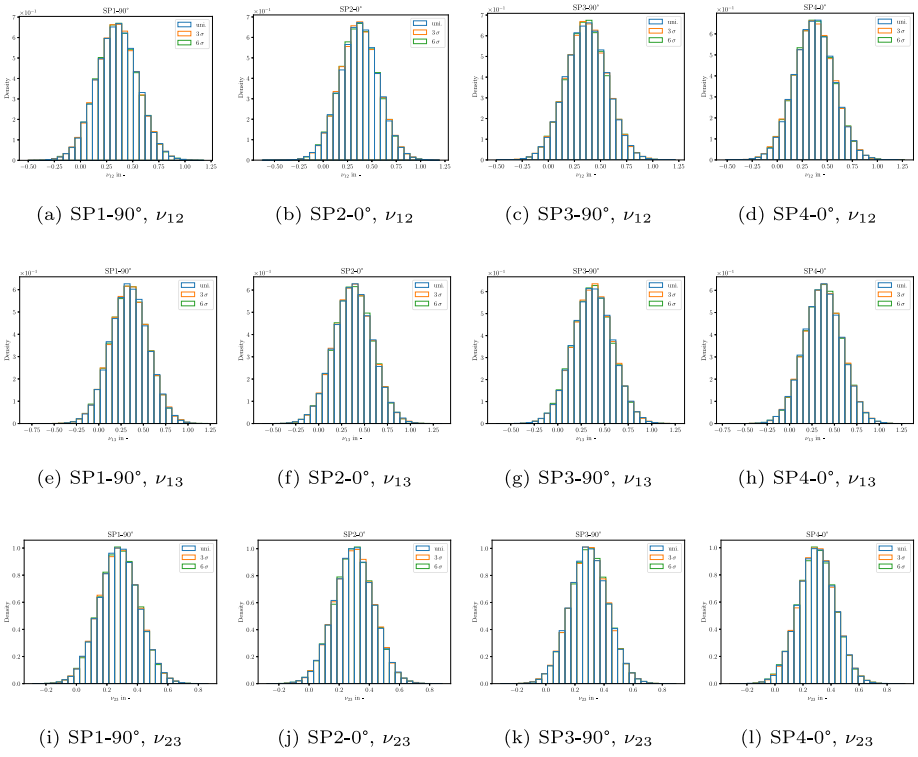

(a) SP1-90°, ν_{12} (b) SP2-0°, ν_{12} (c) SP3-90°, ν_{12} (d) SP4-0°, ν_{12}

(e) SP1-90°, ν_{13} (f) SP2-0°, ν_{13} (g) SP3-90°, ν_{13} (h) SP4-0°, ν_{13}

(i) SP1-90°, ν_{23} (j) SP2-0°, ν_{23} (k) SP3-90°, ν_{23} (l) SP4-0°, ν_{23}

Fig. C.19. Drawn material parameters ν_{12}, ν_{13} and ν_{23} across all structural elements and all simulated cases based on the conditional distribution of the orientation state for different specimen position and injection molding distribution assumptions.

Appendix C. Drawn material parameters

See Figs. C.17–C.19.

Data availability

Data will be made available on request.

References

[1] de Keyser H, Berg L-F, Stammler J. Composite materials ready to replace aluminium in internal combustion engines. JEC Compos Mag 2016;53:32–5.

[2] Aboudi J. Mechanics of composite materials: a unified micromechanical approach. Studies in applied mechanics, vol. 29, Amsterdam and New York: Elsevier; 1991, URL https://www.sciencedirect.com/science/bookseries/09225382/29.

[3] Hashin Z. Analysis of composite materials—a survey. J Appl Mech 1983;50(3):481–505. http://dx.doi.org/10.1115/1.3167081.

[4] Hill R. Elastic properties of reinforced solids: Some theoretical principles. J Mech Phys Solids 1963;11(5):357–72. http://dx.doi.org/10.1016/0022-5096(63)90036-X.

[5] Advani SG, Tucker CL. The use of tensors to describe and predict fiber orientation in short fiber composites. J Rheol 1987;31(8):751–84. http://dx.doi.org/10.1122/1.549945.

[6] Laws N, McLaughlin R. The effect of fibre length on the overall moduli of composite materials. J Mech Phys Solids 1979;27(1):1–13. http://dx.doi.org/10.1016/0022-5096(79)90007-3.

[7] Jiang Z, Liu X, Li G, Lian J. A new analytical model for three-dimensional elastic stress field distribution in short fibre composite. Mater Sci Eng: A 2004;366(2):381–96. http://dx.doi.org/10.1016/j.msea.2003.09.055.

[8] Yu D, Bhattacharyya D. A simple micromechanical approach to predict mechanical behaviour of polypropyl-ene/organoclay nanocomposites based on representative volume element (RVE). Comput Mater Sci 2010;49:1–8.

[9] Wetzel P, Schneider B, Sambale AK, Stommel M, Kaiser J-M. Rve simulations of short fiber reinforced polyamide: Direct and inverse matrix parameter identification in view of the semi-crystalline polymer structure. Compos Sci Technol 2025;260:110961. http://dx.doi.org/10.1016/j.compscitech.2024.110961.

[10] Lusti H. Direct numerical predictions for the elastic and thermoelastic properties of short fibre composites. Compos Sci Technol 2002;62(15):1927–34. http://dx.doi.org/10.1016/S0266-3538(02)00106-9.

[11] Ji B, Wang T. Plastic constitutive behavior of short-fiber/particle reinforced composites. Int J Plast 2003;19(5):565–81. http://dx.doi.org/10.1016/S0749-6419(01)00041-9.

[12] Li M. Proceedings of the 2nd world congress on integrated computational materials engineering. ICME, Cham: Springer International Publishing AG; 2016, URL https://ebookcentral.proquest.com/lib/kxp/detail.action?docID=6367964.

[13] Kärger L, Bernath A, Fritz F, Galkin S, Magagnato D, Oeckerath A, Schön A, Henning F. Development and validation of a cae chain for unidirectional fibre reinforced composite components. Compos Struct 2015;132:350–8. http://dx.doi.org/10.1016/j.compstruct.2015.05.047.

[14] Scrimieri D, Afazov SM, Ratchev SM. An in-core grid index for transferring finite element data across dissimilar meshes. Adv Eng Softw 2015;88:53–62. http://dx.doi.org/10.1016/j.advengsoft.2015.06.001.

[15] Mayer N, van den Broucke B, Prowe J, Havar T, Hinterhölzl R. Finite element mapping for incompatible fe meshes of composite structures. Adv Eng Softw 2016;99:81–8. http://dx.doi.org/10.1016/j.advengsoft.2016.05.007.

[16] Buck F, Brylka B, Müller V, Müller T, Weidenmann KA, Hrymak AN, Henning F, Böhlke T. Two-scale structural mechanical modeling of long fiber reinforced thermoplastics. Compos Sci Technol 2015;117:159–67. http://dx.doi.org/10.1016/j.compscitech.2015.05.020.

[17] Görthofer J, Meyer N, Pallicity TD, Schöttl L, Trauth A, Schemmann M, Hohberg M, Pinter P, Elsner P, Henning F, Hrymak A, Seelig T, Weidenmann K, Kärger L, Böhlke T. Virtual process chain of sheet molding compound: Development, validation and perspectives. Compos B 2019;169:133–47. http://dx.doi.org/10.1016/j.compositesb.2019.04.001.

[18] Reclusado CA, Nagasawa S. Modeling of fiber-reinforced plastics taking into account the manufacturing process. In: Papadrakakis M, editor. Proceedings of the VII European congress on computational methods in applied sciences and engineering. ECCOMAS congress 2016, Athens: Institute of Structural Analysis and Antiseismic Research School of Civil Engineering National Technical University of Athens (NTUA) Greece; 2016, p. 2220–35. http://dx.doi.org/10.7712/100016.1955.5840.

[19] Bijsterbosch H, Gaymans RJ. Polyamide 6—long glass fiber injection moldings. Polym Compos 1995;16(5):363–9. http://dx.doi.org/10.1002/pc.750160504.

[20] Sriramula S, Chryssanthopoulos MK. Quantification of uncertainty modelling in stochastic analysis of frp composites. Compos A 2009;40(11):1673–84. http://dx.doi.org/10.1016/j.compositesa.2009.08.020.

[21] Nguyen BN, Khaleel MA. A mechanistic approach to damage in short-fiber composites based on micromechanical and continuum damage mechanics descriptions. Compos Sci Technol 2004;64(5):607–17. http://dx.doi.org/10.1016/S0266-3538(03)00293-8.

[22] Sharma BN, Naragani D, Nguyen BN, Tucker CL, Sangid MD. Uncertainty quantification of fiber orientation distribution measurements for long-fiber-reinforced thermoplastic composites. J Compos Mater 2018;52(13):1781–97. http://dx.doi.org/10.1177/0021998317733533.

[23] Proy J, Massa F, Notta-Cuvier D, Lauro F, Tison T, Spingler G. Integrating fibers and injection molding process variability in short-natural-fiber-reinforced thermoplastics behavior: A review. Mater Today Commun 2021;29:102785. http://dx.doi.org/10.1016/j.mtcomm.2021.102785, URL https://www.sciencedirect.com/science/article/pii/S2352492821007753.

[24] Hohe J, Paul H, Beckmann C. A probabilistic elasticity model for long fiber reinforced thermoplastics with uncertain microstructure. Mech Mater 2018;122:118–32. http://dx.doi.org/10.1016/j.mechmat.2018.04.007.

[25] Reiner J. A multi-analysis framework for uncertainty quantification and data-driven simulation of design allowables in laminated composites. Compos Sci Technol 2025;261:111030. http://dx.doi.org/10.1016/j.compscitech.2024.111030.

[26] Soize C. Non-gaussian positive-definite matrix-valued random fields for elliptic stochastic partial differential operators. Comput Methods Appl Mech Engrg 2006;195(1–3):26–64. http://dx.doi.org/10.1016/j.cma.2004.12.014.

[27] Rahman S, Chakraborty A. A stochastic micromechanical model for elastic properties of functionally graded materials. Mech Mater 2007;39(6):548–63. http://dx.doi.org/10.1016/j.mechmat.2006.08.006.

[28] Ma J, Zhang S, Wriggers P, Gao W, de Lorenzis L. Stochastic homogenized effective properties of three-dimensional composite material with full randomness and correlation in the microstructure. Comput Struct 2014;144:62–74. http://dx.doi.org/10.1016/j.compstruc.2014.06.003.

[29] Ghauch ZG, Aitharaju V, Rodgers WR, Pasupuleti P, Dereims A, Ghanem RG. Integrated stochastic analysis of fiber composites manufacturing using adapted polynomial chaos expansions. Compos A 2019;118:179–93. http://dx.doi.org/10.1016/j.compositesa.2018.12.029, URL https://www.sciencedirect.com/science/article/pii/S1359835X18305062.

[30] Zaidani M, Omar MA, Kumar S. Coupling of injection molding process to mechanical properties of short fiber composites: A through process modeling approach. J Reinf Plast Compos 2015;34(23):1963–78. http://dx.doi.org/10.1177/0731684415609138.

[31] Mu Y, Chen A, Zhao G, Cui Y, Feng J, Ren F. Prediction for the mechanical property of short fiber-reinforced polymer composites through process modeling method. J Thermoplast Compos Mater 2019;32(11):1525–46. http://dx.doi.org/10.1177/0892705718799815.

[32] Wittemann F, Krauß C, Kärger L. Efficient approximation of varying fiber orientation states in injection molded parts under consideration of multiple manufacturing uncertainties. Appl Compos Mater 2025;32(1):149–72. http://dx.doi.org/10.1007/s10443-024-10268-3.

[33] Rohrmüller B, Christ N, Hohe J, Beckmann C. Numerical study of the microstructure induced uncertainty in the mechanical properties of short fibre reinforced polymers. 9, (8). 2025, http://dx.doi.org/10.3390/jcs9080432,

[34] Ackerman NL, Freer CE, Roy DM. On the computability of conditional probability. J ACM 2019;66(3):1–40. http://dx.doi.org/10.1145/3321699.

[35] Rohrmüller B, Kneisel F, Christ N, Hohe J, Beckmann C. Experimental investigation into the uncertainty of the mechanical properties of short fibre-reinforced polymers. J Compos Sci 2025;9(8). http://dx.doi.org/10.3390/jcs9080432, URL https://www.mdpi.com/2504-477X/9/8/432.

[36] Gandhi UN, Goris S, Osswald TA, Song Y-Y. Discontinuous fiber-reinforced composites: fundamentals and applications. Munich and Cincinnati: Hanser Publishers and Hanser Publications; 2020.

[37] Tucker CL. Fundamentals of fiber orientation: description, measurement and prediction. Munich: Hanser Publishers; 2022, http://dx.doi.org/10.3139/9781569908761, URL https://www.sciencedirect.com/science/book/9781569908754.

[38] Goldberg N, Ospald F, Schneider M. A fiber orientation-adapted integration scheme for computing the hyperelastic tucker average for short fiber reinforced composites. Comput Mech 2017;60(4):595–611. http://dx.doi.org/10.1007/s00466-017-1425-0.

[39] Cintra JS, Tucker CL. Orthotropic closure approximations for flow-induced fiber orientation. J Rheol 1995;39(6):1095–122. http://dx.doi.org/10.1122/1.550630.

[40] Köbler J, Schneider M, Ospald F, Andrä H, Müller R. Fiber orientation interpolation for the multiscale analysis of short fiber reinforced composite parts. Comput Mech 2018;61(6):729–50. http://dx.doi.org/10.1007/s00466-017-1478-0.

[41] Bauer JK, Böhlke T. Variety of fiber orientation tensors. Math Mech Solids 2022;27(7):1185–211. http://dx.doi.org/10.1177/10812865211057602.

[42] Gentle JE, Härdle WK, Mori Y. Handbook of computational statistics. Berlin, Heidelberg: Springer Berlin Heidelberg; 2012, http://dx.doi.org/10.1007/978-3-642-21551-3.

[43] Soch J. Conditional distributions of the multivariate normal distribution. 2020, URL https://statproofbook.github.io/P/mvn-cond.html.

[44] Schneider M. The sequential addition and migration method to generate representative volume ele-ments for the homogenization of short fiber reinforced plastics. Comput Mech 2017;59:247–63.

[45] Schelleis C, Scheuring B, Liebig W, Hrymak A, Henning F. Approaching polycarbonate as an lft-d material: Processing and mechanical properties. Polymers 2023;15:2041. http://dx.doi.org/10.3390/polym15092041.